Aging impairs cold-induced beige adipogenesis and adipocyte metabolic reprogramming

Corey D. Holman[1,2], Alexander P. Sakers[1,2], Ryan P. Calhoun[1,2], Lan Cheng[1,2], Ethan C. Fein[1,2], Christopher Jacobs[3,4], Linus Tsai,[3-5] Evan D. Rosen,[3-5] and Patrick Seale[1,2]

1. Institute for Diabetes, Obesity & Metabolism; Perelman School of Medicine at the University of Pennsylvania, Philadelphia, PA, USA
2. Department of Cell and Developmental Biology; Perelman School of Medicine at the University of Pennsylvania, Philadelphia, PA, USA
3. Division of Endocrinology, Diabetes, and Metabolism, Beth Israel Deaconess Medical Center, Boston, MA, USA
4. Broad Institute of MIT and Harvard, Cambridge, MA, USA
5. Harvard Medical School, Boston, MA, USA

*Correspondence should be addressed to:

Patrick Seale
Perelman School of Medicine
University of Pennsylvania
Smilow Center for Translational Research
3400 Civic Center Blvd, Rm. 12-105
Philadelphia, PA, 19104. USA
Tel: 215-573-8856
Email: sealep@pennmedicine.upenn.edu

Abstract

The energy-burning capability of beige adipose tissue is a potential therapeutic tool for reducing obesity and metabolic disease, but this capacity is decreased by aging. Here, we evaluate the impact of aging on the profile and activity of adipocyte stem and progenitor cells (ASPCs) and adipocytes during the beiging process. We found that aging increases the expression of *Cd9* and other fibro-inflammatory genes in fibroblastic ASPCs and blocks their differentiation into beige adipocytes. Fibroblastic ASPC populations from young and aged mice were equally competent for beige differentiation *in vitro*, suggesting that environmental factors suppress adipogenesis *in vivo*. Examination of adipocytes by single nucleus RNA-sequencing identified compositional and transcriptional differences in adipocyte populations with age and cold exposure. Notably, cold exposure induced an adipocyte population expressing high levels of *de novo* lipogenesis (DNL) genes, and this response was severely blunted in aged animals. We further identified natriuretic peptide clearance receptor *Npr3*, a beige fat repressor, as a marker gene for a subset of white adipocytes and an aging-upregulated gene in adipocytes. In summary, this study indicates that aging blocks beige adipogenesis and dysregulates adipocyte responses to cold exposure and provides a unique resource for identifying cold and aging-regulated pathways in adipose tissue.

Introduction

Brown and beige fat cells are specialized to burn calories for heat production and have the capacity to reduce obesity and metabolic disease. Brown adipocytes are localized in dedicated brown adipose tissue (BAT) depots, whereas beige adipocytes develop in white adipose tissue (WAT) in response to cold exposure, and other stimuli (Wang and Seale, 2016). Adult humans possess thermogenic adipose depots that appear to resemble rodent beige adipose tissue (Jespersen et al., 2013; Wu et al., 2012). Brown and beige adipocytes share similar cellular features such as abundant mitochondria, multilocular lipid droplets, and expression of thermogenic genes like Uncoupling Protein-1 (UCP1). UCP1, when activated, dissipates the mitochondrial proton gradient, leading to high levels of substrate oxidation and heat production (Cannon and Nedergaard, 2004). Brown and beige adipocytes can also produce heat via other UCP1-independent futile cycles (Chouchani et al., 2019).

Increasing beige fat development in mice reduces obesity and improves insulin sensitivity, whereas ablation of beige fat in mice causes metabolic dysfunction (Cederberg et al., 2001; Cohen et al., 2014; Seale et al., 2011; Shao et al., 2016; Stine et al., 2016). Furthermore, transplantation of human beige adipocytes into obese mice reduces liver steatosis and improves metabolic health (Min et al 2016). Beige adipocytes develop via the *de novo* differentiation of adipocyte stem and progenitor cells (ASPCs) or through induction of the thermogenic program in adipocytes (Ferrero et al., 2020; Sakers et al., 2022; Shao et al., 2019).

Human and mouse thermogenic adipose tissue activity declines with aging, predisposing to cardiometabolic disease and limiting the potential of brown/beige fat-targeted therapies (Becher et al., 2021; Berry et al., 2017; Cypess et al., 2012; Rogers et al., 2012; Wang et al., 2019; Yoneshiro et al., 2011). In mice, beige adipose tissue is reduced by ‘middle-age’ (i.e., 1-year-old), preceding many of the damaging effects of old age on organ function (Berry et al., 2017; Goncalves et al., 2017; Rogers et al., 2012). The aging-associated decline in beige fat activity can occur independently of increases in body weight (Rogers et al., 2012; St-Onge, 2005). A variety of processes and pathways have been linked to the aging-induced deficit in beige fat formation, including diminished proliferation and cellular senescence of ASPCs (Berry et al., 2017), increased fibrosis (Wang et al., 2019), increased inflammation (Amiya Kumar Ghosh, 2019), accumulation of anti-adipogenic regulatory cells (Nguyen et al., 2021), and reduced adrenergic tone (Rogers et al., 2012). However, a comprehensive understanding of how cold exposure and aging affect ASPC identity, adipogenesis, and adipocyte phenotypic switching remains elusive.

We applied ASPC lineage tracing, along with unbiased single-cell and single-nucleus RNA sequencing (scRNA-seq; snRNA-seq) to profile the beiging process and evaluate the impact of aging on this process. We found that aging modulates the gene program of multiple fibroblastic ASPC populations and blocks the differentiation of these cells into beige adipocytes *in vivo*. snRNA-seq analysis revealed four types of adipocytes defined by different responses to cold exposure and aging: beige, *Npr3*-high, *de novo* lipogenesis (DNL)-low, and DNL-high. Notably, DNL-high adipocytes were defined by a marked induction of DNL genes during cold exposure in young compared to aged animals. A white adipocyte subpopulation in young mice was marked by expression of Natriuretic peptide receptor-3 (*Npr3*), which was also increased in adipocyte populations from aged mice. Altogether, this study shows that aging blocks cold-stimulated adipocyte reprogramming and ASPC adipogenesis, while implicating suppression of natriuretic peptide signaling and DNL as contributing to the aging-mediated decline in beige fat formation.

Results

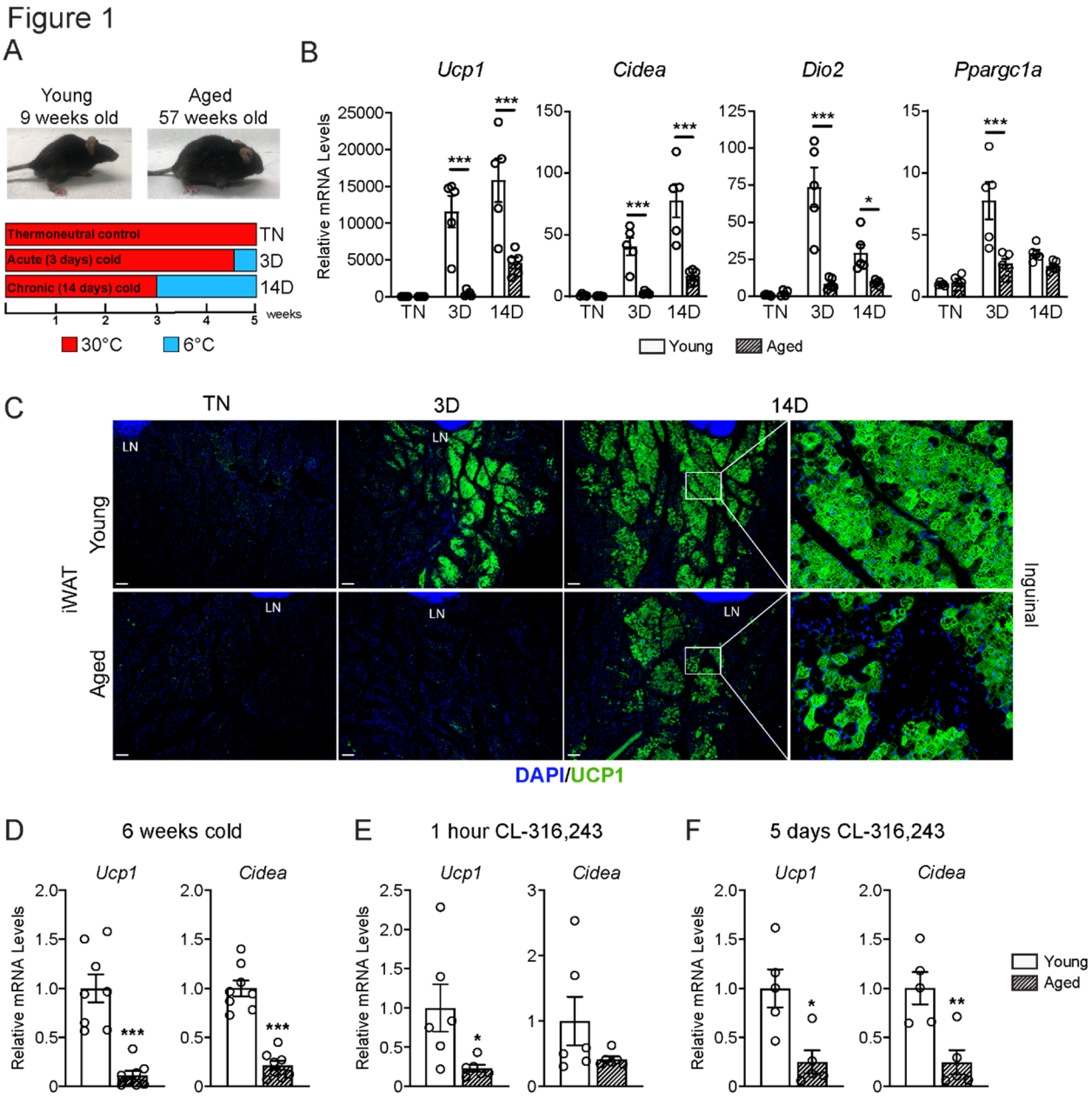

Figure 1. Aged mice exhibit decreased iWAT beiging in response to cold exposure or β3-agonist treatment. (**A**) Young (9-week-old) and aged (57-week-old) C57BL/6 mice were acclimated to 30°C for 3 weeks, followed by two additional weeks either remaining at 30°C (TN, thermoneutral controls), spending the last 3 days at 6°C (3D, acute cold) or last 14 days at 6°C (14D, chronic cold). (**B**) Relative mRNA levels of thermogenic marker genes in mouse iWAT from (A), n=5. (**C**) Immunofluorescence analysis of UCP1 (green) and DAPI (blue) in iWAT sections from mice in (A), LN = lymph node. Scale bar 100 µm. (**D-F**) Relative mRNA levels of *Ucp1* and *Cidea* in iWAT from separate groups of young and aged mice that were either: exposed to 6°C cold for 6 weeks (D), treated with CL-316,243 for 1 hour (E) or treated with CL 316,243 for 5 days (F). Data represent mean ± SEM, points represent biological replicates, 2 groups analyzed using a Student's t-test, and multiple conditions analyzed using a two-way ANOVA with a Tukey correction for multiple comparisons. Significance: not significant, P > 0.05; * P < 0.05 ** P < 0.01; *** P < 0.001.

Aging impairs iWAT beiging

To study the impact of aging on beige adipose tissue development, we exposed young (9-week-old) and middle aged (57-week-old) C57BL/6 mice to 6°C for either 3 or 14 days. All mouse groups were first acclimated to 30°C (thermoneutrality [TN]) for 3 weeks to reduce beige adipose tissue to baseline (low) levels. Following acclimation, TN-housed mice remained at 30°C; acute cold mice (3D) were transitioned to 6°C after 11 days for the final 3 days; and chronic cold mice (14D) were moved to 6°C for two weeks (***Figure 1A***). As expected, the aged mice weighed more and had larger iWAT depots than the young mice (***Figure S1A,B***). Cold exposure greatly and progressively increased the expression levels of thermogenic genes *Ucp1*, *Cidea*, *Dio2* and *Ppargc1a* in young iWAT, and the activation of these genes was significantly blunted in aged mice, especially at the 3D time point (***Figure 1B***). Immunofluorescence (IF) staining showed a robust induction of UCP1 protein in multilocular adipocytes of young iWAT at 3D of cold exposure, which was further increased at 14D. The induction of UCP1^{+} beige adipocytes was severely reduced in aged animals, with strikingly few UCP1+ adipocytes detected. At 14D, the beige adipocytes looked morphologically similar in young and aged mice, though there were fewer in aged animals (***Figure 1C***). At both ages, beige adipocytes were more prominent in the inguinal versus dorsolumbar region of iWAT, consistent with other reports (Barreau et al., 2016; Chi et al., 2018; Dichamp et al., 2019), and beiging was largely absent in the dorsolumbar region of aged mice (***Figure S1C-D, F***). To determine if the beiging response was delayed in aged mice, we exposed young and aged mice at 6°C for 6 weeks. At this time point, the iWAT of aged mice exhibited a larger deficit in thermogenic gene expression compared to young animals (***Figure 1D***). Thermogenic gene levels in interscapular BAT were similar between young and aged mice, at TN and after cold exposure, indicating that the inhibitory effects of aging were selective to WAT (***Figure S1E***).

Next, we examined beige fat formation in young and aged animals upon treatment with the β3-selective adrenergic agonist CL-316,243 (CL). CL acts in an adipose tissue autonomous manner to stimulate beige fat biogenesis, bypassing the central nervous system pathways that mediate the cold response. Acute CL treatment for only 1-hour increased *Ucp1* expression in in iWAT of young mice to a much greater extent than in aged mice (***Figure 1E***). Chronic CL exposure for 5 days also induced much higher expression levels of *Ucp1* and *Cidea* in iWAT of young compared to aged mice (***Figure 1F***). Taken together, these results demonstrate that beige adipose tissue induction is severely impaired in middle aged mice.

Figure 2

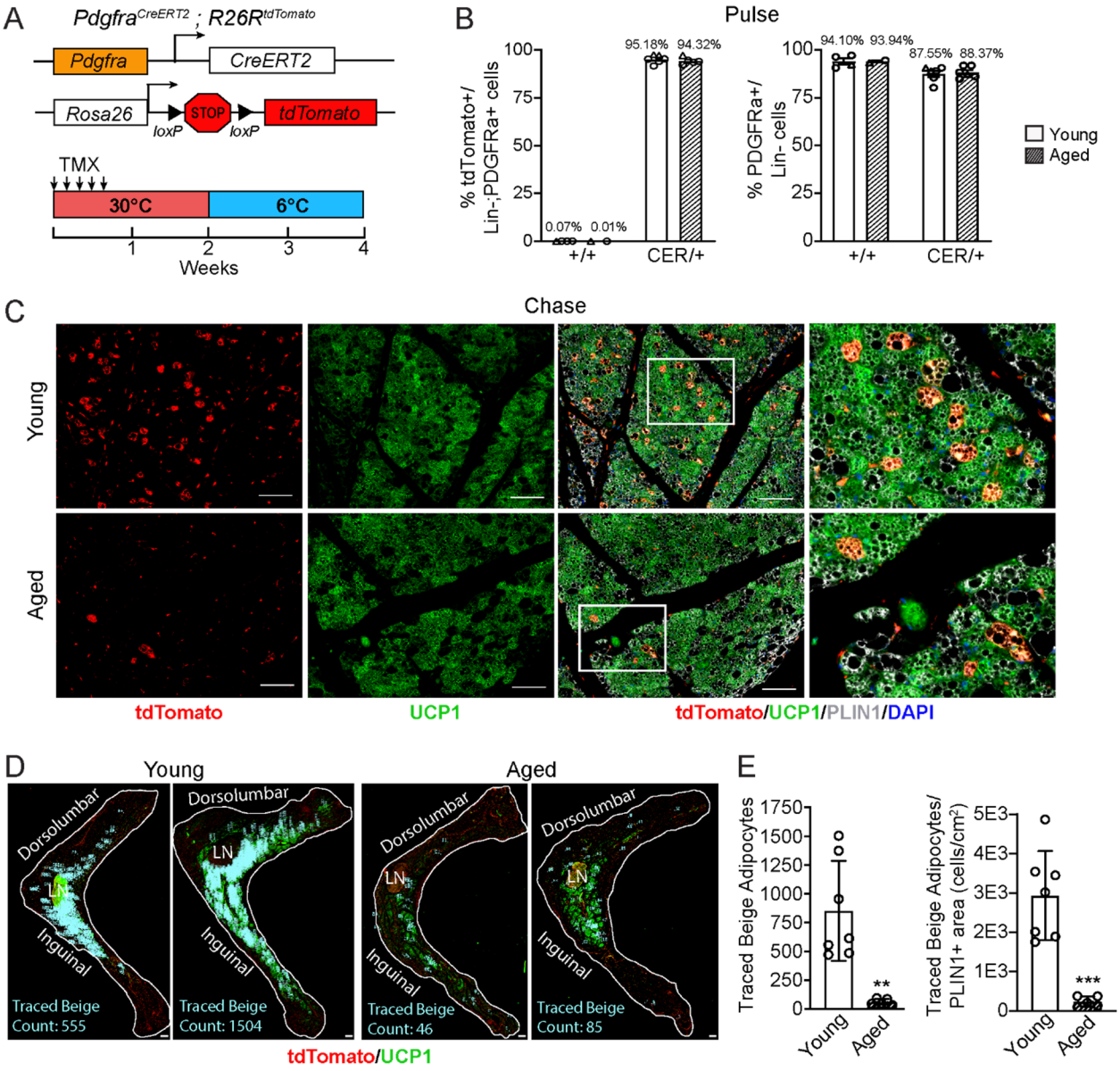

Figure 2. Aging blocks beige adipogenesis from fibroblastic ASPCs.

(**A**) Schematic of *Pdgfra*^{CreERT2};*R26R*^{tdTomato} reporter mouse model and lineage tracing paradigm. (**B**) Flow cytometry-based quantification showing proportions of tdTomato-expressing cells (as % of total Live, Lin- (CD45-/CD31-, PDGFRα^{+} cells) (left) and PDGFRα^{+} cells (as % of total Live, Lin- cells) (right) in iWAT from young and aged Cre^{-} (control, +/+), and Cre+ (CER) mice. n=6 young, 5 aged (Circles represent male mice, triangles represent female mice). (**C**) IF analysis of tdTomato (red), UCP1 (green), PLIN1 (white) and DAPI (blue) in iWAT from young and aged reporter mice after 14 days of 6°C cold exposure (chase). Scale bar 100 μm. (**D**) Representative stitched images of full length iWAT histology slices from samples in (C) showing quantification of traced tdTomato^{+}; UCP1^{+} multilocular (beige) adipocytes (blue numbers). LN= lymph node, scale bar 500 μm. (**E**) Quantification of traced beige adipocytes from (D) presented as total cell number (left) or proportion of PLIN1^{+} area (right), n=7 (young), n=5 (aged). Data represent mean ± SEM, points represent biological replicates, 2 groups analyzed using a

Student's t-test, and multiple conditions analyzed with a two-way ANOVA with a Tukey correction for multiple comparisons. Significance: not significant, P > 0.05; * P < 0.05 ** P < 0.01; *** P < 0.001.

Aging blocks beige adipogenesis from *Pdgfra*$^{+}$ ASPCs

To determine the contribution of fibroblastic ASPCs to beige adipocytes during cold exposure, we performed lineage tracing using *Pdgfra-Cre*^{ERT2};*R26R*^{tdTomato} reporter mice. *Pdgfra* expression marks multiple ASPC populations, including preadipocytes (Merrick et al., 2019; Sakers et al., 2022). Young and aged reporter mice were treated with tamoxifen for 5 days at TN (30°C; "pulse") to activate Cre and induce tdTomato expression in *Pdgfra*$^{+}$ cells. Following a 9 day washout period, mice were transferred to 6°C (cold) for two weeks ("chase") (***Figure 2A***). We observed near complete and specific labeling of ASPCs during the pulse period, with ~95% of PDGFRα^{+} cells in iWAT from young and aged mice displaying tdTomato expression (***Figures 2B, S2A***). The proportion of PDGFRa+ cells in iWAT was similar between young and aged mice (***Figure 2B***). No tdTomato-expressing adipocytes were observed after the pulse (***Figure S2B***). After 14 days of cold exposure, we detected many newly developed beige adipocytes from ASPCs in young mice (visible as tdTomato^{+}/UCP1^{+} multilocular adipocytes). By contrast, very few ASPC-derived (tdTomato^{+}) adipocytes were detected in the beige fat areas of aged iWAT at day 14 (***Figures 2C***). Quantifying across the entire length of iWAT pads revealed that most beige adipogenesis occurred in the inguinal region and was ~12-fold lower in aged compared to young mice (***Figure 2D,E***). However, the overall contribution of *Pdgfra*$^{+}$ ASPCs to beige adipocytes was relatively low, even in young animals, with <20% of beige adipocytes expressing tdTomato.

Figure 3

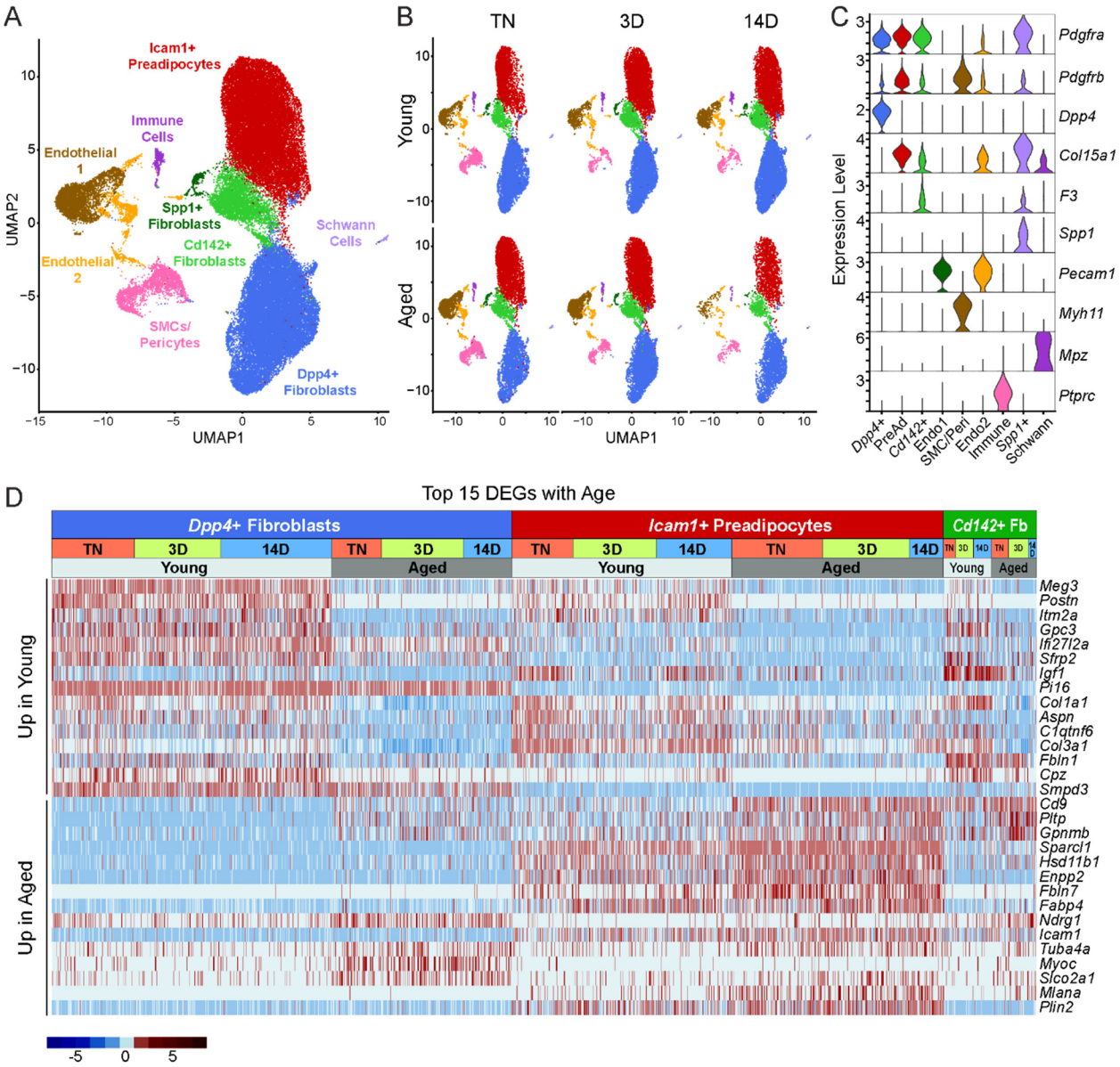

Figure 3. Single cell expression profiling of ASPCs during iWAT beiging.

(**A**) Integrated UMAP of gene expression in 54,987 stromal vascular cells (FACS depleted of CD45$^+$ immune cells) from young and aged mouse groups detailed in Figure 1A. (**B**) UMAPs split by condition. (**C**) Violin plots showing the expression levels of representative marker genes for cell clusters. Y-axis = log-scale normalized read count. (**D**) Expression heatmap of the top differentially expressed genes in young vs. aged fibroblastic ASPCs (combined *Dpp4*$^+$, preadipocytes and *Cd142*$^+$ cells). Table shows expression of these genes in ASPC populations across temperature conditions (TN, cold 3D, cold 14D) from young and aged mice.

Single cell expression profiling of ASPCs

We previously identified three main fibroblastic ASPC populations in iWAT: DPP4$^+$ cells, ICAM1$^+$ preadipocytes, and CD142$^+$ cells. All these cell types express *Pdgfra* and have the capacity to undergo adipogenic differentiation (Merrick et al., 2019). To test whether aging dysregulates one or more of these ASPC types, we performed scRNA-seq on stromal vascular cells from iWAT of young and aged animals, maintained at TN, or following transition to cold for 3 or 14 days (***Figure 1A***). ASPCs were enriched by removing immune (CD45$^+$) cells using fluorescence activated cell sorting (FACS). We integrated the datasets from all conditions together and performed clustering analysis. The following cell populations were annotated based on their expression of cell type-specific marker genes: four fibroblast populations (*Dpp4*$^+$; *Icam1*$^+$ preadipocytes; *Cd142*$^+$, *Spp1*$^+$), two populations of endothelial cells (*Pecam1*$^+$); smooth muscle cells/pericytes (*Myh11*$^+$, *Pdgfrb*$^+$); Schwann cells (*Mpz*$^+$); and residual immune cells (*Ptprc*$^+$) (***Figures 3A-C***). We did not identify any cell population specific to either aging or cold exposure. In this regard, we did not identify 'aging-dependent regulatory cells (ARCs)', which were previously defined as ASPCs expressing *Lgals3* and other inflammatory genes (***Figure S3A***) (Nguyen et al., 2021). The expression levels of identity markers of the ASPC populations were not modulated during cold exposure or aging (***Figure S3B***).

Differential gene expression analyses identified aging-modulated genes in ASPCs (***Figure 3D***). Notably, expression of *Cd9*, previously identified as a fibrogenic marker, was upregulated with age in *Dpp4*$^+$ cells and preadipocytes (Marcelin et al., 2017). *Pltp* and *Gpnmb* were also elevated by aging across all ASPC populations and temperature conditions. Genes downregulated by aging in all ASPC populations included *Meg3*, *Itm2a* and *Gpc3 and Postn*. Of note, *Postn* encodes an extracellular matrix protein that was previously reported to regulate adipose tissue expansion and decrease in expression during aging (Graja et al., 2018).

Figure 4

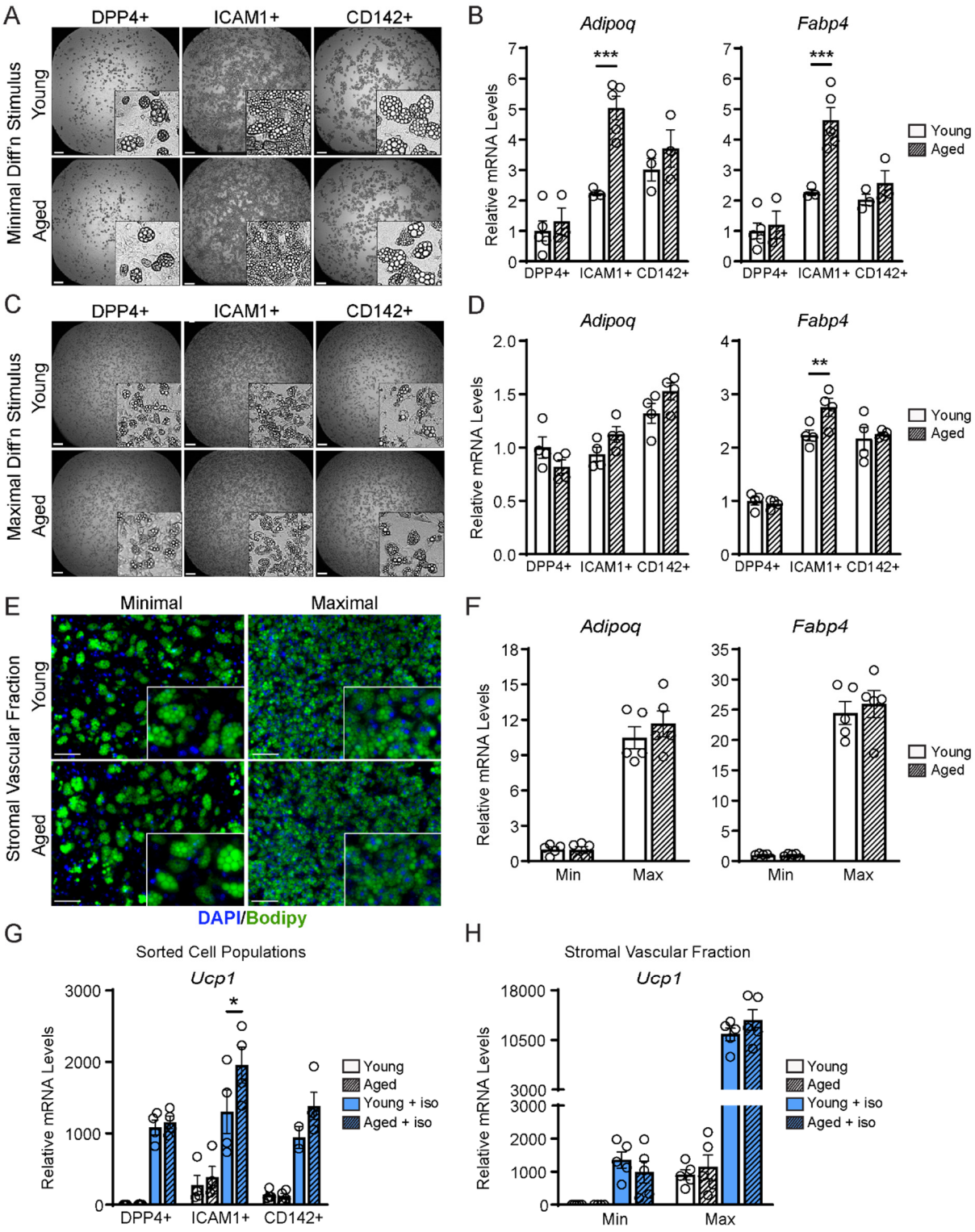

Figure 4. ASPCs from young and aged mice display similar beige adipogenic activity *ex vivo*. (**A, C**) Phase contrast images of DPP4$^+$, ICAM1$^+$ and CD142$^+$ cells from iWAT of young and aged mice that were induced to undergo adipocyte differentiation with minimal (Min, A) or maximal (Max, C) induction cocktail for 8 days. Scale bar 200 µm. (**B, D**) mRNA levels of adipocyte marker genes *Adipoq* and *Fabp4* in cultures from (A, C). Data points represent separate wells, sorted from a pool

of 5 mice (A) or sorted from two pools of 2-3 mice (C). (**E**) Stromal vascular fraction (SVF) cell cultures from the iWAT of young and aged mice were induced to differentiate for 8 days with Minimal or Maximal cocktail, followed by Bodipy (green) staining of lipid droplets and DAPI (blue) staining of nuclei. Scale bar 100 μm. (**F**) Relative mRNA levels of *Adipoq* and *Fabp4* in cultures from (E). Data points represent wells from individual mice, n = 5. (**G, H**) Relative mRNA levels of *Ucp1* in adipocyte cultures from (C, E) with or without treatment with isoproterenol for 4 hours. Data points represent wells sorted from two pools of 2-3 mice (G) or wells from individual mice, n=5 (H). Data represent mean ± SEM, 2 groups analyzed using a Student's t-test, and multiple conditions analyzed with a two-way ANOVA with a Tukey correction for multiple comparisons. Significance: not significant, P > 0.05; * P < 0.05 ** P < 0.01; *** P < 0.001.

ASPCs from aged mice are competent for beige adipogenesis *ex vivo*

We next evaluated if ASPCs from young and aged animals exhibit cell-autonomous differences in adipogenic differentiation capacity. We FACS-purified DPP4$^+$, ICAM1$^+$ and CD142$^+$ cells from the iWAT of young and aged mice, plated them in culture and induced adipocyte differentiation. Using a minimal differentiation stimulus consisting of insulin only (Min), ICAM1$^+$ and CD142$^+$ cells underwent more efficient differentiation into lipid droplet-containing adipocytes, and expressed higher levels of adipocyte genes (*Adipoq* and *Fabp4*) than DPP4$^+$ cells, consistent with prior work (***Figures 4A,B***) (Merrick et al., 2019). DPP4$^+$ and CD142$^+$ cells from young and aged mice underwent adipocyte differentiation and induced adipocyte genes with equivalent efficiency. Unexpectedly, ICAM1$^+$ cells from aged mice exhibited greater differentiation capacity than those from young mice, as evidenced by higher expression levels of *Adipoq* and *Fabp4* (***Figures 4A,B***). Maximal stimulation with a full cocktail of adipogenic inducers (Max) produced similar and robust differentiation in all ASPC populations from young or aged mice (***Figures 4C,D***). To assess whether young and aged ASPCs behave differently when cultured as a mixed heterogeneous population, we isolated the stromal vascular fraction (SVF) for adipogenesis assays. Again, SVF cell cultures from young and aged mice displayed similar adipogenic differentiation efficiency following either Min or Max stimulation (***Figures 4E,F***). Finally, we treated differentiated adipocyte cultures with the pan-adrenergic agonist isoproterenol for 4 hours to evaluate thermogenic gene activation (i.e., beiging). Basal levels of *Ucp1* expression were lower in DPP4$^+$ cells compared to other ASPC types, but all ASPC populations activated *Ucp1* expression to high and similar levels in response to isoproterenol treatment, and did not differ by age (***Figure 4G***). We also did not observe an aging-related difference in the levels of *Ucp1* induction in SVF-derived adipocyte cultures (***Figure 4H***). Together, these data suggest that the beige adipogenic capacity of ASPCs is not intrinsically compromised in aged mice, and therefore the *in vivo* deficit in beige adipogenesis could be due to non-ASPC-autonomous effects.

Figure 5

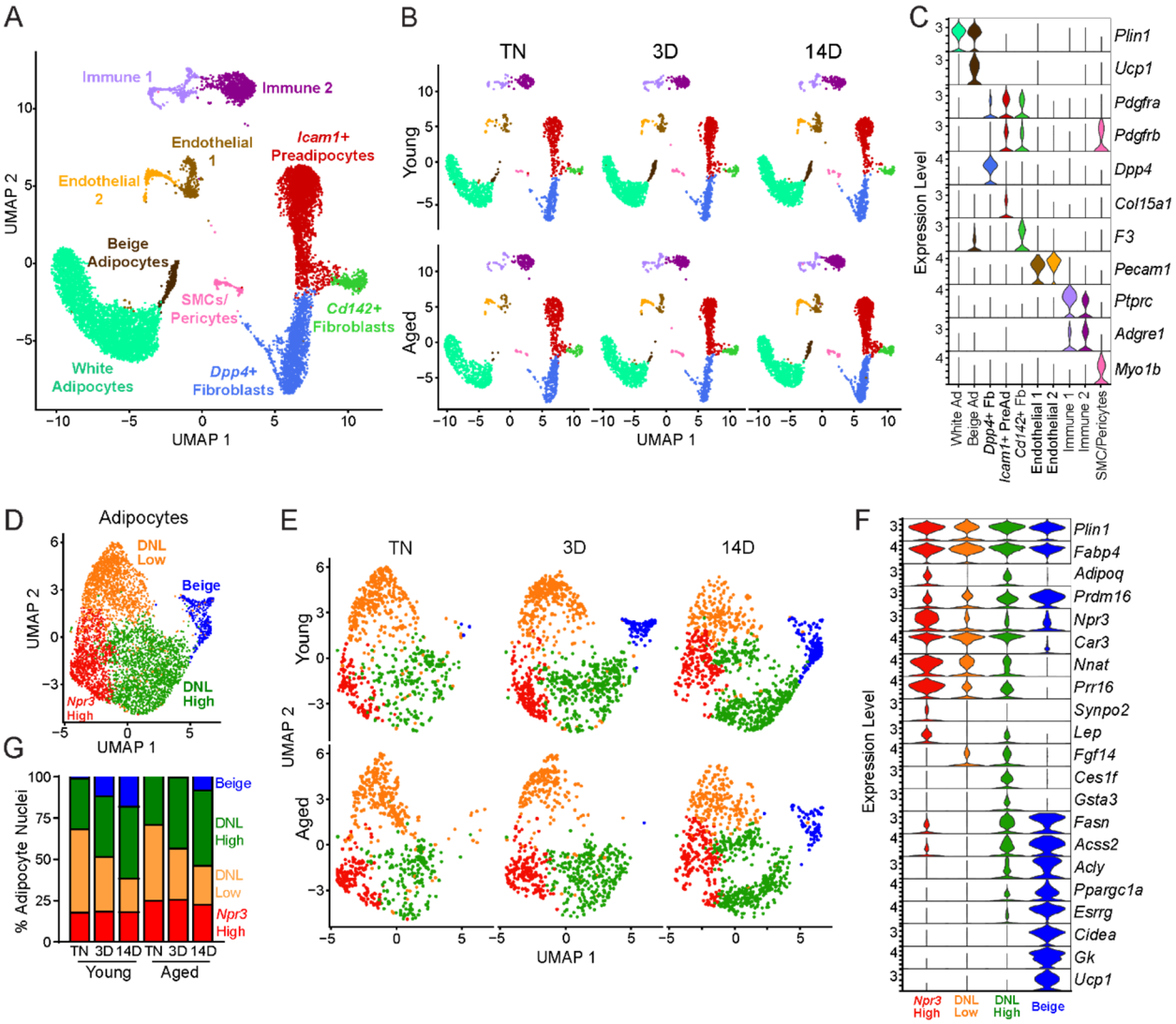

Figure 5. Single nucleus expression profiling of adipocytes during the beiging process in young and aged mice. (**A**) Fully integrated UMAP of mRNA levels in 11,905 nuclei from iWAT of mouse groups detailed in Figure 1A, n=2 mice per condition. (**B**) UMAPs split by condition. (**C**) Violin plots showing expression patterns of cell cluster-selective marker genes, Y-axis = log-scale normalized read count. (**D**) UMAP of gene expression in re-integrated adipocyte clusters including 4,937 nuclei from (A) identifying four populations: *Npr3*-high, beige, DNL-low, and DNL-high. (**E**) Adipocyte UMAPs split by condition. (**F**) Violin plots showing expression patterns of selected genes in adipocyte populations, Y-axis = log-scale normalized read count. (**G**) Adipocyte nuclei numbers in each sample, plotted as percent of total adipocytes captured for that sample.

Single nucleus RNA sequencing uncovers adipocyte heterogeneity

To determine the effects of aging and cold exposure on adipocyte gene profiles, we performed snRNA-seq analyses of iWAT samples using the same experimental paradigm described above (***Figure 1A)***. We integrated all the conditions together for analyses from two separate runs. Similar cell types were captured as with scRNA-seq (***Figure 3A***), but with the addition of mature adipocyte populations (***Figure 5A***). This dataset also has increased representation from immune cells since there was no negative selection against $CD45^+$ cells. As with the single-cell data set, we did not identify any aging-specific cell populations (***Figure S4A***). However, we observed striking gene expression differences in the adipocyte cluster across age and temperature. Most obvious, and expectedly, was the emergence and expansion of a distinct beige adipocyte population, marked by expression of *Ucp1* and other thermogenic genes, during cold exposure (***Figure 5B***).

To focus on adipocyte responses, we reintegrated the snRNA-seq data using only the adipocytes, which revealed four main clusters (***Figures 5D-F***). All adipocyte clusters displayed similarly high mRNA levels of canonical adipocyte markers *Fabp4* and *Plin1*. Beige adipocytes, marked by high expression of many thermogenic genes (i.e., *Ppargc1a*, *Esrrg*, *Cidea*, *Gk, Prdm16* and *Ucp1*), were the most distinctive cluster and were largely absent at TN in young and aged mice. These cells began to appear in young mice after 3 days of cold exposure, and were further increased at 14 days. By contrast, in aged mice, beige cells were barely detectable at 3 days of cold exposure and were present at greatly reduced numbers than in young mice at 14 days (***Figure 5E***). This analysis also revealed three sub-populations of 'white' adipocytes. '*Npr3*-high' adipocytes were enriched for expression of *Npr3*, *Synpo2*, *Prr16*, and *Tshr*, expressed higher levels of white fat marker genes *Leptin* (*Lep*) and *Nnat*, and exhibited the lowest expression levels of thermogenic (beige) genes (Gesta et al., 2007; Rosell et al., 2014). Two additional white adipocyte clusters were designated as '*de novo* lipogenesis (DNL)-low' and 'DNL-high' cells, both of which expressed lower levels of *Npr3* and shared selective expression of *Fgf14.* DNL-high cells uniquely expressed *Ces1f* and *Gsta3* and *activated* high levels of DNL pathway genes (i.e., *Fasn*, *Acss2* and *Acly*) upon cold exposure (***Figure 5F***). Interestingly, Adiponectin (*Adipoq*) was differentially expressed across adipocyte clusters, with higher levels in *Npr3*-high and DNL-high cells. Quantification of adipocyte nuclei from this data set suggested that the proportions of *Npr3*-high and DNL-high adipocytes remain stable across temperature, with aged mice having more *Npr3*-high adipocytes. The proportion of beige adipocytes increased during cold exposure, while DNL-low adipocytes decreased with cold exposure in both young and aged mice (***Figure 5G***).

Figure 6

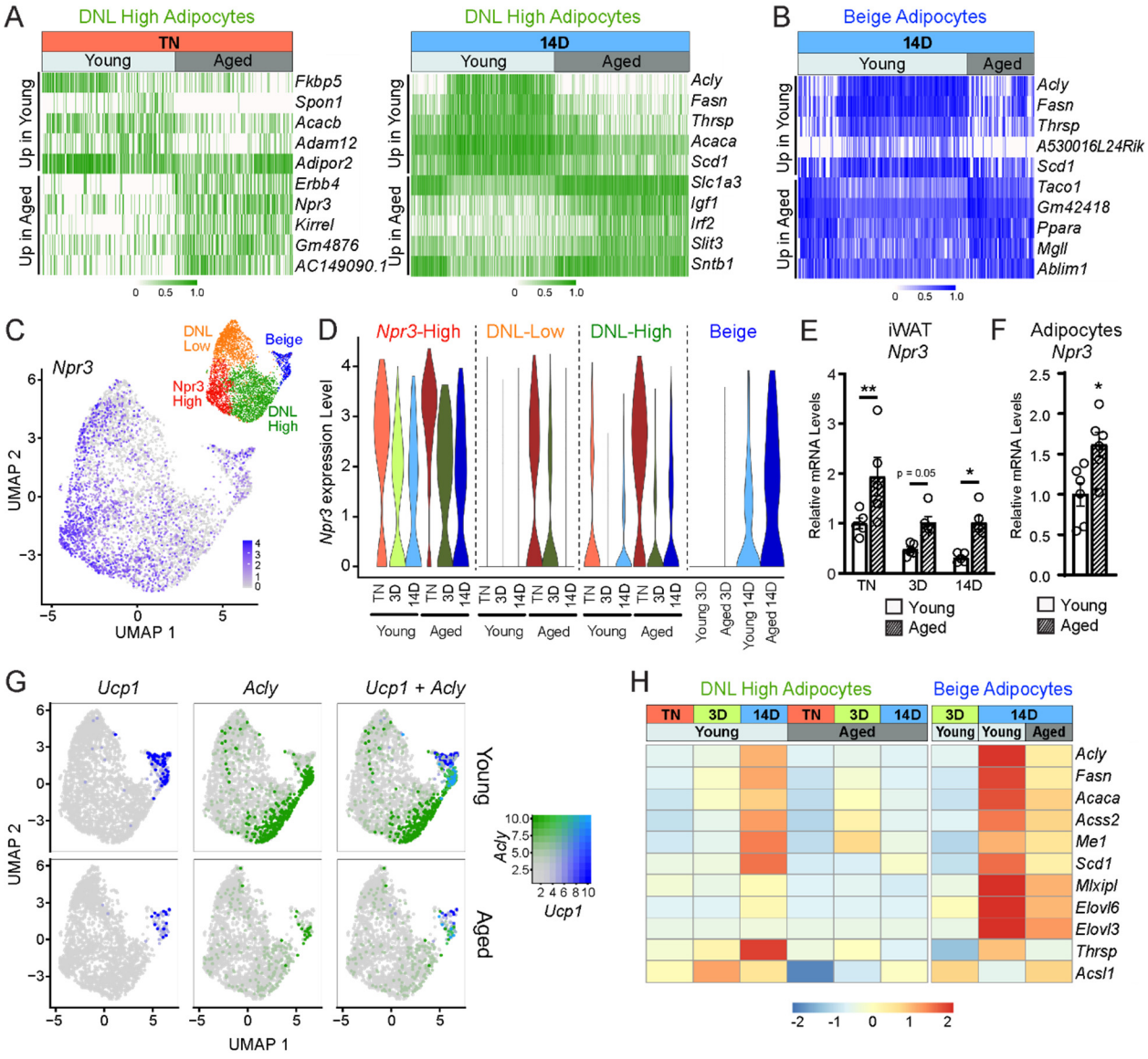

Figure 6. Aging blocks activation of the lipogenic gene program in adipocytes. (**A**) Expression heatmap of the top aging-regulated genes in DNL-high adipocytes at TN (left) and after 14 d of cold exposure (right). (**B**) Expression heatmap of the top aging-regulated genes in beige adipocytes after 14 d of cold exposure. (**C**) UMAP of *Npr3* mRNA levels in adipocyte populations (from Figure 5D). (**D**) Violin plots showing *Npr3* mRNA levels in adipocyte populations at TN (T), and at 3 and 14 days of cold exposure, Y-axis = log-scale normalized read count. (**E**) *Npr3* mRNA levels in iWAT from mouse groups described in Figure 1A, n=5. (**F**) *Npr3* mRNA levels in isolated adipocytes from TN- acclimated young and aged mice, n=6. (**G**) UMAPs of *Ucp1, Acly,* and their co-expression in adipocyte populations from young and aged mice. (**H**) Heatmap showing average expression of DNL genes in all nuclei from DNL-high and beige adipocytes per condition indicated in the top table. Data represent mean ± SEM, points represent biological replicates, 2 groups analyzed using a Student's t-test, and multiple conditions analyzed with a two-way ANOVA with a Tukey correction for multiple comparisons. Significance: not significant, P > 0.05; * P < 0.05 ** P < 0.01; *** P < 0.001.

Aging dysregulates gene programming in adipocyte populations

To evaluate the global effects of cold exposure and aging on adipocytes, we performed differential gene expression analysis between young and aged adipocytes within each cluster. DNL-high and beige adipocytes exhibited the most dramatic expression changes between young and aged animals (***Figures 6A-B, S4B-C***). At TN, DNL-high cells from aged animals expressed lower levels of several genes, including *Fkbp5*, *Spon1* and *Adam12.* Interestingly, *Npr3*, in addition to marking *Npr3*-high cells, was increased by aging in DNL-high adipocytes and to a lesser extent in other adipocyte populations (***Figure 6C,D***). In young animals, *Npr3* expression was downregulated by cold exposure in the three white adipocyte populations, and this downregulation was blunted in aged animals (***Figure 6D***). Gene expression analysis of whole iWAT pads confirmed that *Npr3* mRNA levels were progressively decreased by cold exposure and elevated in aged versus young mice under all temperature conditions (***Figure 6E***). *Npr3* expression levels were also increased in isolated primary adipocytes from aged relative to young mice (***Figure 6F***). Expression levels of the G-protein coupled NP receptors *Npr1* or *Npr2* were not modulated by cold or aging in iWAT or iWAT adipocytes ***(Figure S4D,E).***

We also observed a striking activation of the DNL gene program (*Acly*, *Fasn*, *Acaca*, *Scd1*, etc.) in DNL-high and beige adipocytes during cold exposure (***Figures 6G,H***). The induction of these genes during cold exposure, exemplified by *Acly* expression, was a cluster-defining attribute of DNL-high cells, which did not express beige markers like *Ucp1* even after 14 days of cold exposure. Of note, we found two types of beige (*Ucp1*$^{+}$) adipocytes, distinguished by the presence vs. absence of high DNL gene levels (i.e., *Ucp1*$^{+}$; DNL^{+} and *Ucp1*$^{+}$;DNL($^{-}$)), with the latter arising first during cold exposure (3D vs. 14D) (***Figures 6G, S4F,G***). Importantly, the induction of DNL genes was nearly completely blocked in DNL-high cells and reduced in beige cells of aged animals (***Figure 6G***). Indeed, the top aging downregulated genes in adipocytes from cold exposed mice correspond to DNL and related pathways, especially in DNL-high cells (***Figure S4I)***. Lastly, at the whole tissue level, we observed robust induction of *Acly* in iWAT of young relative to aged mice with increasing duration of cold exposure (***Figure S4H***). Taken together, these results implicate the suppression of natriuretic peptide signaling and DNL in the aging-related impairment of beige fat formation.

Discussion

Thermogenic adipose tissue activity declines during aging of mice and humans, correlating with increases in fat mass and susceptibility to cardiometabolic diseases (Berry et al., 2017; Cypess et al., 2009; Pfannenberg et al., 2010; Rogers et al., 2012; Saito et al., 2009; Wang et al., 2019; Yoneshiro et al., 2011). Our study provides a comprehensive unbiased profile of the adipose tissue beiging process and reveals pathways dysregulated by aging in ASPCs and adipocytes.

Beige adipocytes develop via the *de novo* differentiation of ASPCs or through activation of the thermogenic gene program in mature adipocytes. Previous studies defined three populations of fibroblastic ASPCs in iWAT, namely *Dpp4*$^+$ cells, *Icam1*$^+$ preadipocytes, and *Cd142*$^+$ cells. Aging or cold exposure did not induce dramatic shifts in either the proportions, or gene expression signatures of any of these ASPC types, suggesting that these cell populations are stably maintained across a range of conditions. In support of this, aging did not diminish the cell-intrinsic adipogenic capacities of these ASPC populations, when subjected to adipogenesis assays *ex vivo*. Notably, we did not observe the emergence of aging-dependent regulatory cells (ARCs), previously described as modulated ASPCs co-expressing ASPC and immune marker genes, which have the capacity to suppress adipocyte differentiation (Nguyen et al., 2021). However, we did observe the induction of ARC-selective gene markers (i.e., *Lgals3*, *Cd36*) specifically in immune cells (*Ptprc*$^+$, *Adgre1*$^+$) from aged mice in both our scRNA-seq and snRNA-seq datasets. This *Lgals3*/*Cd36* gene signature has also been described in Lin$^+$ macrophages and CD45$^+$ lipid-associated (LAM) macrophages (Burl et al., 2018; Jaitin et al., 2019). Overall, our results suggest that aging-induced alterations to the systemic milieu or adipose tissue environment are responsible for the block in beige adipogenesis.

Gene expression analyses identified several genes that were altered by aging across multiple ASPC types and temperature conditions. The top aging-upregulated gene was *Cd9*, which was previously identified as a marker of fibrogenic (fibrosis-generating) progenitor cells (Marcelin et al., 2017). *Cd9* encodes for a tetraspanin protein implicated in various processes that could affect adipogenesis, including extracellular vesicle production, cell adhesion, inflammation, and platelet activation (Brosseau et al., 2018). Aging also upregulated the expression of *Pltp* and *Gpnmb*, which are both linked to the regulation of inflammation and fibrosis (Prabata et al., 2021; Saade et al., 2021). Conversely, *Meg3*, *Itm2a* and *Postn* were consistently downregulated across all ASPC populations from aged versus young mice. Of note, Periostin (*Postn*) is an extracellular matrix protein that regulates adipose tissue lipid storage, and its levels were previously shown to decrease in several adipose tissue depots during aging (Graja et al., 2018).

We were surprised by the limited (<20%) contribution of fibroblastic (*Pdgfra*$^+$) ASPCs, (which includes *Pparg*-expressing preadipocytes), to beige adipocytes during cold exposure. Of note, we also observed tdTomato$^+$, unilocular white adipocytes upon cold exposure, suggesting the bi-potential fate of *Pdgfra*$^+$ cells. Previous studies in mice using an adipocyte fate tracking system show that a high proportion of beige adipocytes arise via the *de novo* differentiation of ASPCs as early as 3 days of cold (Wang et al., 2013). However, the relative contribution from ASPC differentiation and direct adipocyte conversion to the formation of beige adipocytes depends highly on the experimental conditions, especially cold exposure history (Shao et al., 2019). Mice housed at TN from birth undergo high rates of *de novo* beige adipogenesis upon first cold exposure, whereas mice reared at room temperature acquire many 'dormant' beige adipocytes that can be re-activated by cold exposure (Rosenwald et al., 2013; Shao et al., 2019). Based on these findings, we presume that mature (dormant beige) adipocytes serve as the major source of beige adipocytes in our cold-exposure paradigm. However, long-term cold exposure also recruits smooth muscle cells to differentiate into beige adipocytes; a process that we did not investigate here (Berry et al., 2016; Long et al., 2014; McDonald et al., 2015; Shamsi et al., 2021).

The beiging process is associated with a dramatic remodeling of adipose tissue structure and metabolic function. We applied snRNA-seq analysis to investigate the cold response of iWAT adipocytes in young and aged animals, leading us to identify four adipocyte clusters: beige adipocytes and three "white" subsets: *Npr3*-high, DNL-low and DNL-high adipocytes. *Npr3*-high adipocytes were enriched for expression of white fat-selective genes and exhibit the lowest levels of thermogenic genes (Rosell et al., 2014; Ussar et al., 2014). Interestingly, *Npr3* also upregulated by aging in all white adipocytes. Previous studies show that obesity also increases *Npr3* levels in adipose tissue of mice and humans (Gentili et al., 2017; Kovacova et al., 2016). NPR3 represses beige fat development and adipocyte thermogenesis by functioning as a clearance receptor for natriuretic peptides (NPs), thereby reducing their lipolytic and thermogenic effects (Bordicchia et al., 2012; Coue et al., 2018; Moro et al., 2004; Sengenès et al., 2000; Sengenes et al., 2003). Together, these results suggest that *Npr3*-high adipocytes may impede beige fat development in a cell non-autonomous manner by reducing NP signaling. Moreover, high NPR3 levels in aged animals could contribute to the block in beige fat development, and targeting this pathway may be a promising avenue to elevate beige fat activity.

We were also intrigued by the dramatic induction of DNL genes in beige adipocytes and DNL-high cells during cold exposure. Previous work established that cold stimulates opposing pathways of lipid oxidation and lipogenesis in thermogenic fat tissue (Mottillo et al., 2014; Sanchez-Gurmaches et al., 2018; Yu et al., 2002). The co-occurrence of these two processes is

unusual and may provide a mechanism to ensure the continued availability of fatty acids to fuel thermogenesis and/or provide critical metabolic intermediates, such as acetyl-CoA. The Granneman lab demonstrated that high expression of the lipid catabolic enzyme MCAD and lipogenic enzyme FAS occurred in separate populations of iWAT adipocytes upon stimulation with a β3-adrenergic agonist for 3-7 days (Lee et al., 2017). We identified two subsets of UCP1$^+$ beige adipocytes, distinguished by the presence vs. absence of high levels of DNL genes (i.e., *Ucp1*$^+$; DNL-high and *Ucp1*$^+$; DNL-low). Interestingly, the *Ucp1*$^+$; DNL-high cells accumulated later during cold exposure (14D), suggesting that fully cold-adapted beige adipocytes express both pathways simultaneously. Of note, the induction of *Acly* and other lipogenic genes was very severely impaired in aged animals. Related to this point, Martinez Calejman and colleagues showed that *Acly* deficiency in brown adipocytes caused a whitened phenotype, coupled with an unexpected and unexplained reduction in *Ucp1* expression (Martinez Calejman et al., 2020). We speculate that high levels of ACLY may be required to support thermogenic gene transcription by supplying and efficiently shuttling acetyl-CoA for acetylation of histones or other proteins.

Aging is a complex process, and unsurprisingly, many pathways have been linked to the aging-related decline in beiging capacity. For example, increased adipose cell senescence, impaired mitochondrial function, elevated PDGF signaling and dysregulated immune cell activity during aging diminish beige fat formation (Benvie et al., 2023; Berry et al., 2017; Goldberg et al., 2021; Nguyen et al., 2021). Of note, older mice exhibit higher body and fat mass, which is associated with metabolic dysfunction and reduced beige fat development. While the effects of aging and altered body composition are difficult to separate, previous studies suggest that the beiging deficit in aged mice is not solely attributable to changes in body weight (Rogers et al., 2012). Further studies, including additional time points across the aging continuum may help clarify the role of aging and ascertain when beiging capacity decreases.

In summary, this work shows that aging impairs beige adipogenesis through non-cell-autonomous effects on adipose tissue precursors and by disrupting adipocyte responses to environmental cold exposure. Expression profiling at the single-cell level reveals adipocyte heterogeneity, including two different types of UCP1$^+$ beige adipocytes. Finally, aging-dysregulated pathways, including natriuretic peptide signaling and lipogenesis, may provide promising targets for unlocking beige adipocyte development.

Acknowledgements

We thank members of the Seale lab for helpful advice and discussions.

Funding: NIH grants DK120982 and DK121801 to P.S.; T32 HD083185 to C.D.H; T32 DK007314 to E.F.; RC2 DK116691 to E.D.R.

Author Contributions: C.D.H, A.P.S, R.C. and P.S. were responsible for conceptualization and data analysis. C.D.H and P.S were responsible for writing of the manuscript. C.D.H and A.P.S conducted the majority of the experiments. R.C. and E.F. performed bioinformatics analyses. L.C. processed tissue sections for histology and performed immunostaining. C.J., L.T., and E.D.R. performed and processed the snRNA-seq experiment.

Competing Interests: The authors declare no competing interests.

Data and materials availability: scRNA-seq and snRNA-seq datasets are deposited in the Gene Expression Omnibus (GEO) under the superseries accession number GSE227441.

Data analysis pipelines used for processing of raw sequencing data, integration and clustering can be obtained from: https://github.com/calhounr/Aging-impairs-cold-induced-beige-adipogenesis-and-adipocyte-metabolic-reprogramming

Supplemental Figures

Figure S1

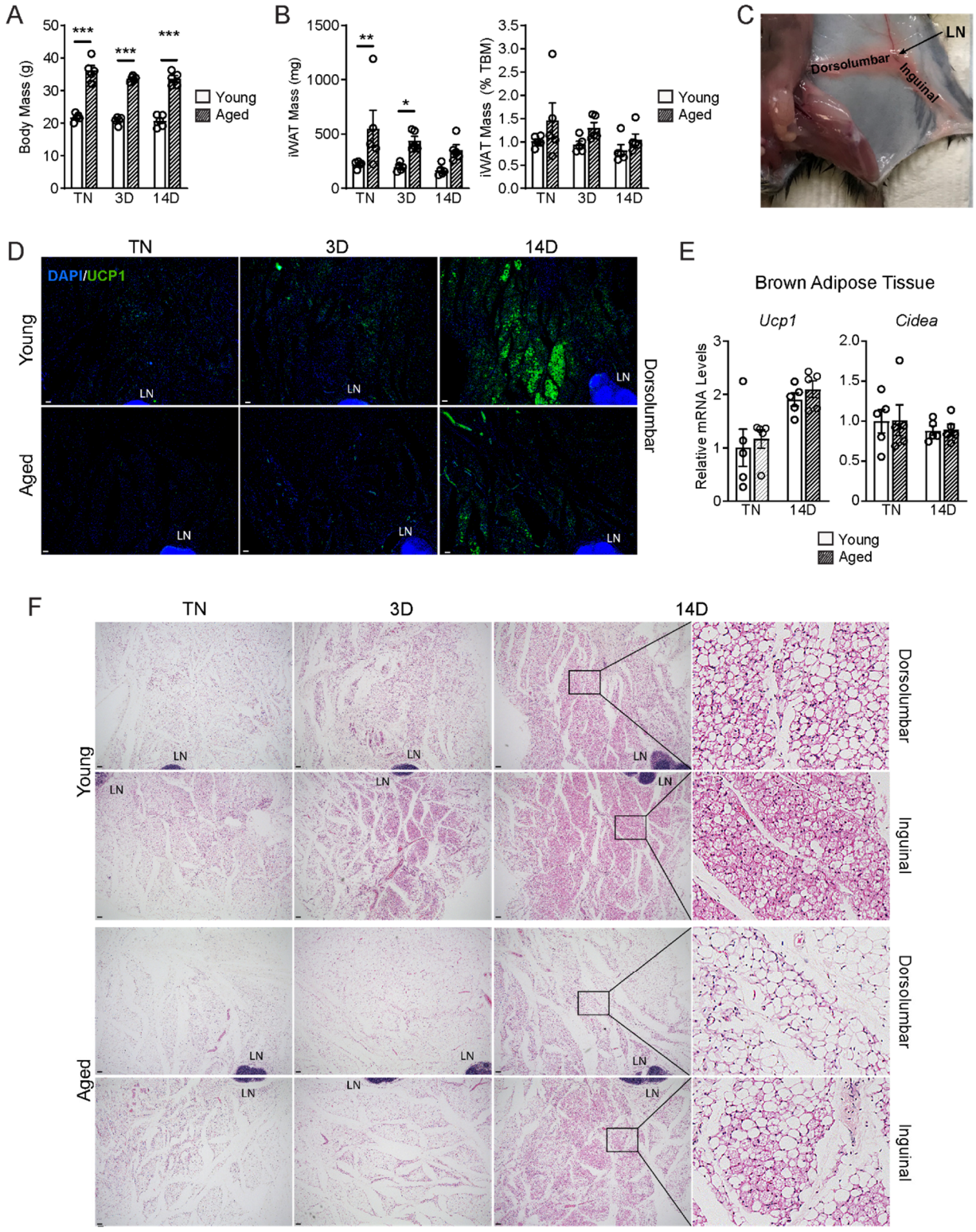

Figure S1, related to Figure 1. (**A-B**) Body mass and iWAT mass of mice described in Figure 1A, n=5. (**C**) Mouse dissection with lymph node (LN) orientation showing the dorsolumbar and inguinal regions of the iWAT pad. (**D**) Immunofluorescence analysis of iWAT with UCP1 (green) and DAPI (blue). LN=lymph node. Scale bar 100 µm. (**E**) mRNA levels of *Ucp1* and *Cidea* in BAT of young and aged mice housed at TN, and either maintained at TN or exposed to cold for 2 weeks. (**F**) H&E staining of serial sections of iWAT from D (above) and Figure 1C, LN=lymph node. Scale bar 100 µm. Data represent mean ± SEM, points represent biological replicates, analyzed using a Student's t-test with a two-way ANOVA with a Tukey correction for multiple comparisons. Significance: not significant, P > 0.05; * P < 0.05 ** P < 0.01; *** P < 0.001.

Figure S2

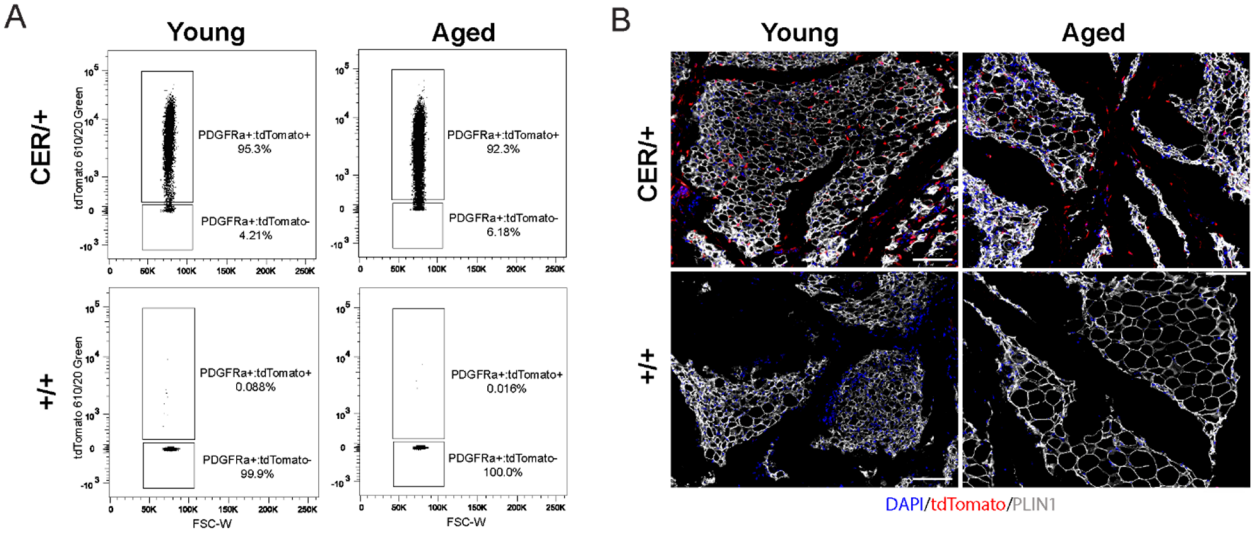

Figure S2, related to Figure 2. (**A**) Representative flow cytometry plots showing expression of tdTomato in gated Live, Lin^-; $PDGFR\alpha^+$ stromal vascular cells isolated from young and aged reporter mice (described in Figure 2) immediately after treatment with tamoxifen (tmx, pulse). (**B**) Immunofluorescence analysis of iWAT from young and aged reporter mice with tdTomato (red), PLIN1 (white) and DAPI (blue) after the tmx pulse, scale bar 100 µm.

Figure S3

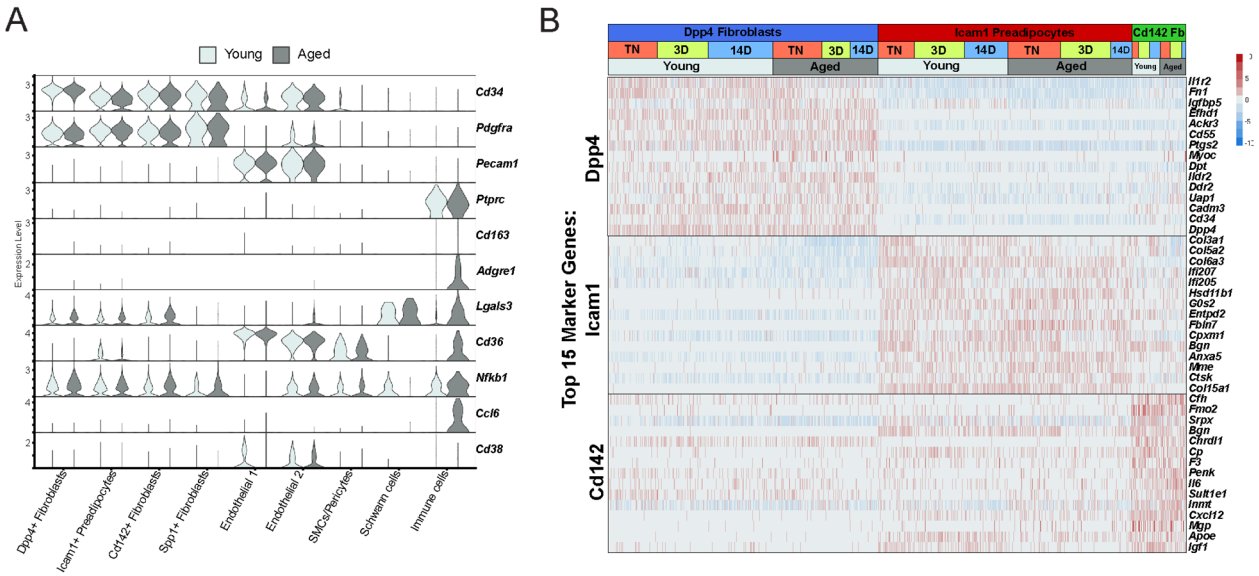

Figure S3, related to Figure 3. (**A**) Violin plot showing expression of ARC marker genes in cell clusters split by age, Y-axis = log-scale normalized read count. (**B**) Expression heatmap of top ASPC marker genes across age and housing conditions.

Figure S4

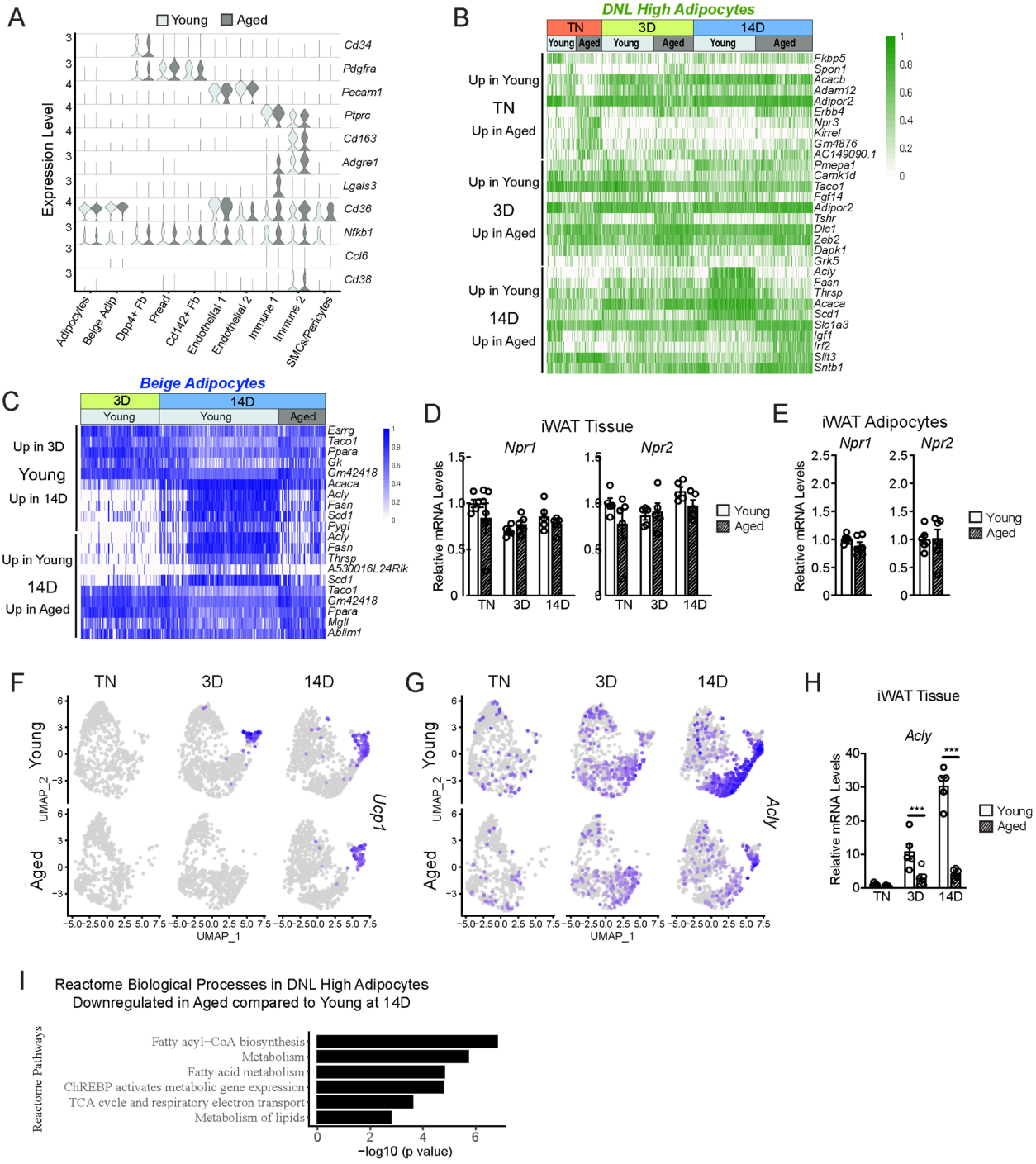

Figure S4, related to Figures 5,6. (**A**) Violin plot showing expression levels of ARC marker genes split by age, y-axis = log-scale normalized read count. (**B**) Expression heatmap of the top aging-regulated genes in DNL-high adipocytes. (**C**) Expression heatmap of the top aging-regulated and cold-regulated genes in beige adipocytes. (**D-E**) *Npr1* and *Npr2* mRNA levels in (D) iWAT from mouse groups described in Figure 1A, n=5 and (E) isolated adipocytes from iWAT from TN-acclimated young and aged mice, n=6. (**E-F**) UMAP of *Ucp1* (E) and *Acly* (F) mRNA levels in adipocyte populations (from Figure 5D). (**H**)

Acly mRNA levels in iWAT from mouse groups described in Figure 1A, n=5. (**G**) Enrichment analysis displaying the top six Reactome pathways in DNL high adipocytes downregulated in aged at 14 days. Data represent mean ± SEM, points represent biological replicates, 2 groups analyzed using a Student's t-test, and multiple conditions analyzed with a two-way ANOVA with a Tukey correction for multiple comparisons. Significance: not significant, P > 0.05; * P < 0.05 ** P < 0.01; *** P < 0.001.

Materials and Methods

Key Resources Table

Reagent type (species) or resource	Designation	Source or reference	Identifiers	Additional information
genetic reagent (M. *musculus*)	C57BL/6J	The Jackson Laboratory, Bar Harbor, ME	RRID:IMSR_JAX:000664	
genetic reagent (M. *musculus*)	C57BL/6JN	NIA, Bethesda, MD	NA	
genetic reagent (M. *musculus*)	Rosa26 loxp-stop-loxp tdTomato Reporter (Ai14)	The Jackson Laboratory, Bar Harbor, ME	RRID:IMSR_JAX:007914	
genetic reagent (M. *musculus*)	$Pdgfra^{CreERT2}$	The Jackson Laboratory, Bar Harbor, ME	RRID:IMSR_JAX:032770	
antibody	Rabbit anti–red fluorescent protein (RFP)	Rockland, Pottstown, PA	600-401-379, RRID:AB_2209751	1:500
antibody	Rabbit anti-Perilipin (D418)	Cell Signaling, Denvers, MA	3470, RRID:AB_2167268	1:200
antibody	Rabbit anti- UCP1	Specially made by AstraZeneca, Cambridge, UK	NA	1:2000
antibody	Anti-mouse CD142	Sino Biological, Chesterbrook, PA	50413- R001	1:100
antibody	Anti-mouse CD142	R & D Systems, Minneapolis, MN	AF3178, RRID:AB_2278143	1:50
antibody	Anti-mouse CD140a-(PDGFRα)-PECy7	Biolegend, San Diego, CA	135912, RRID:AB_2715974	1:100
antibody	Anti-mouse-CD31 (APC-Fire)	Biolegend, San Diego, CA	102528, RRID:AB_2721491	1:1000
antibody	Anti-mouse CD45-allophycocyanin (APC/Cy7)	Biolegend, San Diego, CA	103116, RRID:AB_312981	1:1000
antibody	Anti-mouse ICAM1-phycoerythrin (PE/Cy7)	Biolegend, San Diego, CA	116122, RRID:AB_2715950	1:100
antibody	Anti-mouse CD26 (DPP-4)-fluorescein isothiocyanate (FITC)	Biolegend, San Diego, CA	137806, RRID:AB_10663402	1:200
sequence-based reagent	mTbp	PMID: 24703692	NA	F-GAAGCTGCGGTACAATTCCAG R-CCCCTTGTACCCTTCACCAAT
sequence-based reagent	mAdipoq	PMID: 24703692	NA	F-GCACTGGCAAGTTCTACTGCAA R-GTAGGTGAAGAGAACGGCCTTGT

sequence-based reagent	mFabp4	PMID: 24703692	NA	F-ACACCGAGATTTCCTTCAAACTG R-CCATCTAGGGTTATGATGCTCTTCA
sequence-based reagent	mCidea	PMID: 24703692	NA	F-TGCTCTTCTGTATCGCCCAGT R-GCCGTGTTAAGGAATCTGCTG
sequence-based reagent	mPgc1a	PMID: 24703692	NA	F-CCCTGCCATTGTTAAGACC R-TGCTGCTGTTCCTGTTTTC
sequence-based reagent	mUcp1	PMID: 24703692	NA	F-ACTGCCACACCTCCAGTCATT R-CTTTGCCTCACTCAGGATTGG
sequence-based reagent	mDio2	PMID: 24703692	NA	F-CAGTGTGGTGCACGTCTCCAATC R-TGAACCAAAGTTGACCACCAG
sequence-based reagent	mAcly	PMID: 31141698	NA	F-GAGTGCTATTGCGCTTCCC R-GGTTGCCGAAGTCACAGGT
sequence-based reagent	mNpr3	This Paper	NA	F-TTTTCAGGAGGAGGGGTTGC R-ACACATGATCACCACTCGCT
sequence-based reagent	mNpr1	MGH PrimerBank	Primer Bank ID: 113930717c1	F-GCTTGTGCTCTATGCAGATCG R-CCTCGACGAACTCCTGGTG
sequence-based reagent	mNpr2	MGH PrimerBank	Primer Bank ID: 118129825c2	F-CATGACCCCGACCTTCTGTTG R-CGAACCAGGGTACGATAATGCT
commercial assay or kit	ABI High-Capacity cDNA Synthesis kit	Applied Biosystems, Waltham, MA	4368813	
commercial assay or kit	Purelink RNA Mini columns	Invitrogen, Waltham, MA	LT-12183018	
commercial assay or kit	TSA TMR Tyramide Reagent Pack	Akoya Biosciences, Marlborough, MA	NEL742001KT	
commercial assay or kit	TSA Fluorescein Tyramide Reagent Pack	Akoya Biosciences, Marlborough, MA	NEL741001KT	
commercial assay or kit	Bulls Eye Decloaking Buffer	Biocare, Pacheco, CA	BULL1000 MX	
commercial assay or kit	AbC Total Antibody Compensation Bead Kit	BioLegend,San Diego, CA	A10497	
commercial assay or kit	Biotium Mix-n-Stain CF647	Sigma, Burlington, MA	MX647S100	
commercial assay or kit	PicoPure RNA Isolation Kit	Invitrogen, Waltham, MA	KIT0204	
commercial assay or kit	Qubit dsDNA High Sensitivity assay kit	ThermoFisher, Waltham, MA	Q32851	
commercial assay or kit	DNA High Sensitivity Bioanalyzer Chip (Agilent)	Agilent, Santa Clara, CA	5067-4626	
software, algorithm	Graphpad Prism	Graphpad, San Diego, CA	RRID:SCR_002798	
software, algorithm	Adobe Illustrator	Adobe, San Jose, CA	RRID:SCR_010279	
software, algorithm	Adobe Photoshop	Adobe, San Jose, CA	RRID:SCR_014199	
software, algorithm	Image J	PMID: 22743772	RRID:SCR_003070	
software, algorithm	Cell Ranger	10x Genomics	RRID:SCR_017344	
software, algorithm	Seurat	PMID: 34062119	RRID:SCR_016341	
software, algorithm	bcl2fastq	Illumina	RRID:SCR_015058	

software, algorithm	Cumulus	PMID: 32719530	RRID:SCR_021644	
software, algorithm	FACSDiva Softward	Becton Dickinson, Franklin Lakes, NJ	RRID:SCR_001456	
other	Tamoxifen (Free Base)	Sigma, Burlington, MA	T5648	
other	Corn Oil	Sigma, Burlington, MA	C8267	
other	16% Paraformaldehyde	EMS, Hatfield, PA	15710	
other	TRIzol	Invitrogen, Waltham, MA	15596018	
other	CL-316,243	Sigma, Burlington, MA	C5976	
other	4',6-Diamidine-2'-phenylindole dihydrochloride (DAPI), 1:10,000	Roche, Basel, Switzerland	10236276001	
other	Bovine Serum Albumin, fraction V, fatty-acid free	Gold Biotechnology, St. Louis, MO	A-421-250	
other	DMEM/F12	Fisher Scientific, Waltham, MA	11320033	
other	Fetal Bovine Serum	Omega Scientific, Tarzana, CA	FB-11, Lot 401714	
other	Primocin	InvivoGen, San Diego, CA	ant-pm-2	
other	PCR Master Mix, Power SYBR Green	Applied Biosystems, Waltham, MA	4367659	
other	HBSS, 1X	Fisher Scientific, Waltham, MA	14175079	
other	Dispase II	Roche, Basel, Switzerland	4942078001	
other	Collagenase, Type 1	Worthington, Lakewood, NJ	LS004197	
other	Red Blood Cell Lysis Buffer, 10x	BioLegend, San Diego, CA	420302	
other	Human Insulin, Novolin	Novo Nordisk, Bagsvaerd, Denmark	183311	
other	Dexamethasone	Sigma-Aldrich, Burlington, VT	D4902	
other	3-isobutyl-1-methylxanthine (IBMX)	Sigma-Aldrich, Burlington, VT	I7018	
other	Rosiglitazone	Cayman Chemical, Ann Arbor, MI	11884	
other	Indomethacin	Sigma-Aldrich, Burlington, VT	I8280	
other	3,30,5-Triiodo-L-thyronine sodium salt (T3)	Sigma-Aldrich, Burlington, VT	T6397	
other	isoproterenol	Sigma-Aldrich, Burlington, VT	I6504	
other	Biodipy 493/503	Invitrogen, Waltham, MA	D3922	
other	Hoechst 33342	Thermo Fisher, Waltham, MA	62249	
other	Protector RNase Inhibitor	Roche, Basel, Switzerland	3335399001	

464

Mice

All animal procedures were approved and performed under the guidance of the University of Pennsylvania Institutional Animal Care and Use Committee. Young (4 weeks) and aged (52 weeks) C57BL/6 male mice were obtained from the National Institute of Aging (C57BL/6JN) or Jackson Laboratories (C57BL/6J, stock number 000664). Mice were housed at 30°C for 3 weeks, then were either: maintained at 30°C for 2 weeks (TN); kept at 30°C for 11 more days before moving to 6°C for 3 days (3D cold) or moved to 6°C for 14 days (14D cold). Mice were single housed during the final two week temperature treatment and provided with a nestlet and shepherd shack. For experiments with CL316,243 (CL, Sigma-C5976), mice were housed at 30°C for 5 weeks, followed by intraperitoneal (IP) injection of 1 mg/kg/d CL either 1 hour prior to tissue harvest or for 5 days. *Pdgfra*^{CreERT2} mice were obtained from Dr. Brigid Hogan (Duke University) (Chung et al., 2018) and crossed with *Rosa26*^{tdTomato} (strain: B6.Cg-Gt(ROSA)26Sortm14(CAG-tdTomato)Hze/J, stock no. 007914). To induce Cre activity, tamoxifen (Sigma, T5648) dissolved in corn oil (Sigma, C8267) was injected intraperitonially (IP) into mice at a dose of 100 mg/kg/d for 5 days. For all iWAT processing other than histology, the inguinal lymph node was removed.

Histology and Immunofluorescence

Tissues were fixed overnight in 4% paraformaldehyde, washed with PBS, dehydrated in ethanol, paraffin-embedded and sectioned. Following deparaffinization, slides were subjected to heat antigen retrieval in a pressure cooker with Bulls Eye Decloaking buffer (Biocare), unless otherwise noted. Slides were incubated in primary antibody overnight and secondary antibody conjugated to peroxidase and then developed using Tyramide Signal Amplification (TSA, Akoya Biosciences). Samples were stained with either hematoxylin and eosin or the following antibodies: anti-red fluorescent protein (RFP) (rabbit; 1:500; Rockland #600-401-379), anti-UCP1 (rabbit, 1:2000, AstraZeneca), and anti-PLIN1 (rabbit, 1:200 Cell Signaling #3470). Slides were imaged on an inverted fluorescence microscope (Keyence BZ-X710). For quantification of tdTomato-expressing adipocytes, full-length iWAT slices were tile imaged, stitched, exported as a BigTiff, and quantified using the Count Tool in Photoshop (Adobe).

Isolation of stromal vascular cells (SCVs) and adipocytes

SVCs. As previously described (Merrick et al 2019, Wang et al 2019), iWAT tissue was dissected, minced gently and digested with Collagenase Type I (1.5 units/ml; Worthington) and Dispase II (2.4 units/ml; Roche) in DMEM/F12 containing 1% fatty acid-free bovine serum albumin (Gold Biotechnology) in a gentleMACS dissociator (Miltenyi Biotec) on program “37 MR ATDK-1.” The

digestion was quenched with DMEM/F12 containing 10% FBS, and the dissociated cells were passed through a 100 µm filter and spun at 400 x g for 4 mins. The pellet was resuspended in red blood cell lysis buffer (BioLegend), incubated for 4 mins at RT, then quenched with DMEM/F12 containing 10% serum. Cells were passed through a 70 µm filter, spun, resuspended, then passed through a final 40 µm filter, spun at 400 x g for 4 minutes and plated or underwent further processing for FACS. Mice were not pooled unless indicated.

Adipocytes. Tissue went through the same process as above, except after digestion and quenching, adipocyte/SVF slurry was filtered through a 200 µm filter and centrifuged at 50 x g for 3 mins at RT. Using a 20 mL syringe and 1.5-inch, 25G needle, media containing the SVCs was removed from below the adipocytes (and saved if concurrently isolating SVCs), leaving only the adipocytes in the tube. Adipocytes were washed twice with the same media as quenching, transferred to 2 mL tubes, spun a final time, media was removed from below the adipocytes again, and TRIzol was added for RNA extraction. Mice were not pooled.

FACS

DPP4$^+$, ICAM1$^+$, and CD142$^+$ cells were isolated as previously described (Merrick et al 2019). Briefly, SVCs from the subcutaneous adipose of mice (n= 2-5) were pooled and resuspended in FACS buffer (HBSS containing 3% FBS; Fisher), then incubated for 1 hr at 4°C with the following antibodies: CD26 (DPP4)-fluorescein isothiocyanate (FITC) (Biolegend, 137806; 1:200), anti-mouse ICAM1-phycoerythrin (PE)/Cy7 (Biolegend, 116122; 1:100), anti-mouse CD45-allophycocyanin (APC)/Cy7 (Biolegend, 103116; 1:1000), anti-mouse CD31-APC-Fire (Biolegend, 102528; 1:1000), and anti-mouse CD142 (Sino Biological, 50413-R001, 1:100; or R&D Systems, AF3178, 1:50). Anti-mouse CD142 antibodies were conjugated with Biotium Mix-n-Stain CF647 (Sigma, MX647S100). For lineage tracing pulse analysis, SVCs were isolated from individual mice without pooling. SVCs were stained with anti-mouse CD31, anti-mouse CD45, and anti-mouse CD140a (PDGFRA) (PE/Cy7) (Biolegend, 135912; 1:100). In all FACS experiments, cells were stained with 4′,6-diamidino-2-phenylindole (DAPI) (Roche, 10236276001; 1:10,000) for 5 minutes, then washed three times with FACS buffer to remove unbound antibodies. Cells were sorted with a BD FACS Aria cell sorter (BD Biosciences) equipped with a 100 µm nozzle and the following lasers and filters: DAPI, 405 and 450/50 nm; FITC, 488 and 515/20 nm; mTomato, 532 and 610/20 nm; PE/Cy7, 532 and 780/60 nm; CF647, 640 and 660/20 nm; and APC/Cy7 and APC-Fire, 640 and 780/60 nm. All compensation was performed at the time of acquisition in Diva software by using compensation beads (BioLegend, A10497) for single-color staining and SVCs for negative staining and fluorescence (DAPI and tdTomato).

Cell culture and differentiation

Adipocyte precursor cells. All cells were cultured in DMEM/F12 containing 10% FBS and Primocin (50 ng/ml) (InvivoGen, ant-pm-1). $DPP4^+$, $ICAM1^+$, and $CD142^+$ populations were FACS purified, plated on CellBind 384-well plates (Corning) at 15-25K cells/well, and incubated for 48 (25K cells) to 72 hours (15K cells) to facilitate attachment before the induction of adipogenic differentiation. For whole SVF, SVCs were isolated and plated in a 48 well CellBind plate (Corning) at a high confluency of one mouse per 18 wells. No cells were passaged after plating to maintain adipogenic competency. Differentiation was carried out with either maximum adipogenic cocktail, max: 500 µM isobutylmethylxanthine (Sigma, I7018), 10 µM dexamethasone (Sigma, D4902), 125 µM indomethacin (Sigma, I8280), 1 µM rosiglitazone (Cayman Chemical, 11884), 1 nM T3 (Sigma, T6397), and 20 nM insulin (Novolin) or a minimal adipogenic cocktail, min: 20 nM insulin. For the max adipogenic cocktail induction, cells were incubated with cocktail for 2 days and then transferred to adipogenic maintenance medium for the remaining 6 days (1 µM rosiglitazone, 1 nM T3, and 20 nM insulin). For all conditions, medium was changed every 2 days, and cells were harvested on day 8 of differentiation. For drug treatments, cells were treated for 4 hrs on day 8 with 1 µM isoproterenol (Sigma, I6504). Adipogenesis was assessed by staining with Biodipy 493/503 (Invitrogen, D3922) for lipid droplet accumulation and Hoechst 33342 (Thermo Fisher, 62249) for nuclei number. The cells were imaged on a Keyence inverted fluorescence microscope (BZ-X710) by using DAPI (excitation, 360/40 nm; emission, 460/50 nm) and green fluorescent protein (excitation, 470/40 nm; emission, 525/50 nm) filters. Individual wells were imaged in their entirety at 4x magnification, and at 20x to see morphology. 384-well plates were not stained and imaged in brightfield due to low cell number recovery from FACS prior to RNA extraction.

RNA Extraction, qRT-PCR and RNA Sequencing

RNA Extraction. Total RNA was extracted using TRIzol (Invitrogen) combined with PureLink RNA Mini columns (Thermo Fisher, 12183025) for tissue and SVC cells or by PicoPure RNA Isolation Kit (Applied Biosystems, KIT0204) for 384-well plate populations and adipocytes. Prior to the addition of chloroform, all tissue and primary adipocytes in TRIzol included an extra spin at max speed for 10 minutes at RT, then TRIzol was removed from below the lipid layer to avoid lipid contamination disrupting the subsequent phase separation with chloroform. Chloroform was added to the lipid-free TRIzol, spun for 15 mins at 12,000 x g and the aqueous layer was removed and added to columns. mRNA was quantified using a Nanodrop and reverse transcribed to cDNA using the ABI High-Capacity cDNA Synthesis kit (ABI, 4368813). Real-time PCR was performed

on a QuantStudio5 qPCR machine using SYBR green fluorescent dye (Applied Biosystems). Fold changes were calculated using the ddCT method, with TATA binding Protein (*Tbp*) mRNA serving as a normalization control.

Single Cell RNA-seq Samples. Cells were flow sorted to isolate live ($DAPI^-$) cells and remove debris. We enriched non-immune cells by sorting out $CD45^+$ cells. Next-generation sequencing libraries were prepared using the Chromium Next GEM Single Cell 3' Reagent kit v3.1 (10x Genomics, 1000121) per manufacturer's instructions. Libraries were uniquely indexed using the Chromium Single Index Kit T Set A, pooled, and sequenced on an Illumina NovaSeq 6000 sequencer in a paired-end, dual indexing run by the CHOP Center for Applied Genomics at the University of Pennsylvania. Sequencing for each library targeted 20,000 mean reads per cell.

Single Nucleus RNA-seq Samples.

Nuclei were isolated from frozen mouse iWAT samples as previously described, with the following modifications to integrate hash multiplexing and FANS-assisted nuclear quality thresholding and sample pooling (Drokhlyansky et al., 2020; Slyper et al., 2020). Briefly, 300 mg of flash-frozen adipose samples were held on dry ice until immediately before nuclei isolation, and all sample handling steps were performed on ice. Each sample was placed into a gentleMACS C tube (Miltenyi Biotec, 130-093-237) with 2 mL freshly prepared TST buffer (0.03% Tween 20 (Bio-Rad), 0.01% Molecular Grade BSA (New England Biolabs), 146 mM NaCl (ThermoFisher Scientific), 1 mM $CaCl_2$ (VWR International), 21 mM $MgCl_2$ (Sigma Aldrich), and 10 mM Tris-HCl pH 7.5 (ThermoFisher Scientific) in ultrapure water (ThermoFisher Scientific)) with 0.2 U/µL of Protector RNase Inhibitor (Sigma Aldrich, RNAINH-RO). gentleMACS C tubes were then placed on the gentleMACS Dissociator (Miltenyi Biotec) and tissue was dissociated by running the program "mr_adipose_01" three times, and then incubated on ice for 10 minutes. Lysate was passed through a 40 µm nylon filter (CellTreat) and collected into a 50 mL conical tube (Corning). Filter was rinsed with 3 mL of freshly prepared ST buffer (146 mM NaCl, 1 mM $CaCl_2$, 21 mM $MgCl_2$; 10 mM Tris-HCl pH 7.5) with 0.2 U/µL RNase Inhibitor, and collected into the same tube. Flow-through was passed through a 20 µm pre-separation filter (Miltenyi Biotec) set on top of a 5 mL FACS tube (Corning) and collected into the same tube. Suspension was centrifuged in a swinging-bucket centrifuge (Eppendorf) at 500 × g for 5 minutes at 4°C with brake set to low. Following centrifugation, supernatant was removed and 5 mL of PBS pH 7.4 (ThermoFisher Scientific) with 0.02% BSA and 0.2 U/µL RNase Inhibitor was added without resuspending the nuclear pellet. Sample was centrifuged again at 500 × g for 5 minutes at 4°C with brake set to low. Following

centrifugation, supernatant was removed, and the nuclear pellet was resuspended in 1 mL PBS-0.02% BSA with 0.2 U/μL RNase Inhibitor. Each sample was split into two 500 μL aliquots and transferred to new 5 mL FACS tubes for subsequent hashing. Each aliquot of resuspended nuclei was stained with NucBlue (ThermoFisher, R37605), labeled with 1 μg of a unique TotalSeq anti-Nuclear Pore Complex Proteins Hashtag Antibody (Biolegend), and then incubated on ice for 30 minutes. Suspension was centrifuged at 500 × g for 5 minutes at 4°C with brake set to low. Following centrifugation, 450 μL of supernatant was removed and the nuclear pellet was resuspended in 450 μL PBS-0.02% BSA with 0.2 U/μL RNase Inhibitor. For nuclear quality thresholding, fluorescence-activated nuclear sorting (FANS) was implemented to collect 4,000-4,300 nuclei from hashtagged aliquots directly into a shared well of a 96-well PCR plate (Thermo Scientific) containing 24.6 μL of 10X RT Reagent B with 1U/uL RNase Inhibitor on a Beckman Coulter MoFlo AstriosEQ fitted with a 70 μm nozzle. High-quality nuclei were selected by initial gating at 360 nm with laser filter 405-448/59 followed by SSC-H and FSC-H to remove doublets and unlysed cells. Once all sample aliquots were FANS-sorted, the pool of 43,000 nuclei was loaded on the 10x Chromium controller (10x Genomics) according to the manufacturer's protocol. cDNA and gene expression libraries were generated according to the manufacturer's instructions (10x Genomics). Libraries of hashtag oligo fractions were generated according to the manufacturer's instructions (Biolegend). cDNA and gene expression library fragment sizes were assessed with a DNA High Sensitivity Bioanalyzer Chip (Agilent). cDNA and gene expression libraries were quantified using the Qubit dsDNA High Sensitivity assay kit (ThermoFisher, Q32854). Gene expression libraries were multiplexed and sequenced on the Nextseq 500 (Illumina) using a 75-cycle kit and the following read structure: Read 1: 28 cycles, Read 2: 55 cycles, Index Read 1: 8 cycles.

Bioinformatics analysis

Single Cell RNA Sequencing

Data was processed using the Cell Ranger pipeline (10x Genomics, v.3.1.0) for demultiplexing and alignment of sequencing reads to the mm10 transcriptome and creation of feature-barcode matrices. The cell ranger output files were read into R (version 4.1.1) and processed utilizing the standard Seurat CCA integrated workflow (version 4.3.0). Each of the six samples went through a first phase of filtering, where only cells that recorded more than 200 features and only features present in a minimum of 3 cells were kept. Each sample was filtered prior to downstream analysis on nCount_RNA, nFeature_RNA, and mitochondrial percentages. Samples were then normalized using a LogNormalization method with a scaling factor of 10000 followed by FindVariableFeatures

using Variance Stabilization Transformation with the top 6000 features to be returned. The samples were scored on their cell cycle phases which would be used in the regression later. The FindIntegrationAnchors function using the CCA reduction method and IntegrateData was utilized to integrate the data together. The integrated data-set was then scaled in which mitochondrial percentage and cell cycle state was regressed out. A principal component analysis was performed and the top 15 dimensions were kept. Uniform Manifold and Projection (UMAP) was run on the dataset, in addition to FindNeighbors and FindClusters. Differential gene expression between clusters was performed using the FindMarkers function with the Wilocox test in Seurat. Violin plots and individual UMAP plots were all generated using the Seurat toolkit VlnPlot and FeaturePlot functions, respectively. Heatmaps were generated utilizing the pheatmap package (version 1.0.12).

Single Nucleus RNA Sequencing

Raw sequencing reads were demultiplexed to FASTQ format files using bcl2fastq (Illumina; version 2.20.0). Digital expression matrices were generated from the FASTQ files using Cell Ranger (Zheng et al., 2017)(version 6.1.2) with the option to include intronic reads (--include-introns). Reads were aligned against the GRCm38 mouse genome assembly and gene counts were obtained, per-droplet, by summarizing exonic and intronic UMIs that overlapped with the GENCODE mouse annotation (release 24) for each gene symbol. In order to adjust for downstream effects of ambient RNA expression within mouse nuclei, we used the "remove-background" module from CellBender (Fleming et al., 2022) (version 0.2.0) to remove counts due to ambient RNA molecules from the count matrices and to estimate the true cells. Genes were subsequently filtered such that only genes detected in two or more cells and with at least 6 total counts (across all cells) were retained. Sample demultiplexing via hashtag oligonucleotide sequences (HTOs) was performed with the Cumulus sc/snRNA-Seq processing pipeline (Li et al., 2020). Specifically, HTO quantification was performed with the Cumulus Tool on Feature Barcoding, which provided a cell-by-HTO count matrix. This HTO count matrix, along with the gene count matrices generated via Cell Ranger (above) were used to assign each cell to their respective sample(s) with the demuxEM program. Only cells that were identified as singlets were retained (i.e. no cells identified as a multiplet or unassignable) in the per-sample CellBender-ed gene count matrices.

Cellbender output files were read into R (version 4.1.1) and processed utilizing the standard Seurat CCA and later RPCA integration workflows (version 4.3.0). Each of the hashed samples (24 in total) were merged with their respective pair to have a total of twelve samples

consisting of six different groups. Each sample was filtered prior to downstream analysis based on their nCount_RNA, nFeature_RNA, and mitochondrial percentages. Samples were then normalized using a LogNormalization method with a scaling factor of 10000 followed by FindVariableFeatures using a Variance-Stabilizing Transformation as the method with the top 2000 features to be returned. The FindIntegrationAnchors function using the CCA reduction method and IntegrateData was utilized to integrate the data together. The integrated data-set was then scaled on which mitochondrial percentage was regressed. A principal component analysis was performed in which only the top 18 dimensions were retained. Uniform Manifold and Projection (UMAP), FindNeighbors, and FindClusters with a resolution of 0.4 was performed on the dataset. To remove doublets in the dataset, we used the package scDblFinder (1.8.0) and their function scDblFinder with the parameters of samples set to our twelve samples, dbr set to NULL, dbr.sd set to 1, clusters set to FALSE, and multiSampleMode set to split. The object was then subsetted to only contain expected singlets. Differential gene expression between clusters was performed using the FindMarkers function with the Wilocox test in Seurat. Violin plots and individual UMAP plots were all generated using the Seurat toolkit VlnPlot and FeaturePlot functions, respectively. Heatmaps were generated utilizing the dittoSeq package (1.9.1) and pheatmap package (version 1.0.12).

After identifying the adipocyte population, we subsetted our object on that population, extracting the raw RNA counts on the cells for each of the six samples (YTN, OTN, Y3D, O3D, Y14D, O14D) (Y is young, O is “Old” or as referred to in this paper, Aged). These samples were then integrated together using the standard RPCA integration workflow. There was no further filtering done on the reintegrated adipocyte population. Samples were normalized using a LogNormalization method with a scaling factor of 10000 followed by FindvariableFeatures using a Variance-Stabilizing Transformation as the method with the top 2000 features to be returned. The function SelectIntegrationFeatures was performed on the dataset where it was then scaled on which mitochondrial percentage was regressed, and principal components were found using the ScaleData and RunPCA functions. The FindIntegrationAnchors function using the ROCA reduction method and a k.anchors of 20 and IntegrateData was utilized to integrate the data together. After integration, the dataset was then scaled in which mitochondrial percentage was regressed on again. A principal component analysis was performed in which only the top 18 dimensions were retained. Uniform Manifold and Projection (UMAP), FindNeighbors, and FindClusters with a resolution of 0.2 was performed on the dataset. Differential gene expression between clusters was performed using the FindMarkers function with a Wilcoxon signed-rank test as the method in Seurat. Violin plots and individual UMAP plots were all generated using the

Seurat toolkit VlnPlot and FeaturePlot functions, respectively. Heatmaps were generated utilizing the dittoSeq package (1.9.1) and pheatmap package (version 1.0.12).

Enrichment analysis was performed on the positively expressed genes with a $\log_2$ fold change (LFC) > 0.25 and a $P_{adjusted}$ value < 0.01 on comparison of the young 14 days cold and old 14 days cold groups in the DNL high cluster. The generated gene list, which was in order of significance, was fed into g:Profiler (version 0.2.1) using default parameters except with modifications to query as an ordered query against the 'mmusculus' database, a gSCS correction method for multiple testing, with domain scope set to annotated, and sources set to the Reactome database. The top six enriched pathways yielded from the database were taken and displayed in order of $P_{adjusted}$ value.

Statistical methods

All bar graphs represent the mean ± SEM. A Student's t-test was used when 2 groups were compared. Where multiple conditions were compared, we applied two-way ANOVA with a Tukey correction for multiple comparisons. Only the Young vs. Aged comparisons were depicted on graphs for clarity, with additional multiple comparisons provided below. P values are indicated by asterisks and defined as *p < 0.05, **p < 0.01 and ***p < 0.001. All statistics were calculated with GraphPad Prism Version 10.0.3.

Figure	Graph	Statistical Test	Comparison	P value
1B	*Ucp1* qPCR	2 way ANOVA with a Tukey correction for multiple comparisons	3D: Young vs. Aged	<0.001
			14D: Young vs. Aged	<0.001
			Young: TN vs. 3D	<0.001
			Young: TN vs. 14D	<0.001
1B	*Cidea* qPCR	2 way ANOVA with a Tukey correction for multiple comparisons	3D: Young vs. Aged	<0.001
			14D: Young vs. Aged	<0.001
			Young: TN vs. 3D	<0.001
			Young: TN vs. 14D	<0.001
			Young: 3D vs. 14D	0.001
1B	*Dio2* qPCR	2 way ANOVA with a Tukey correction for multiple comparisons	3D: Young vs. Aged	<0.001
			14D: Young vs. Aged	0.03
			Young: TN vs. 3D	<0.001
			Young: TN vs. 14D	0.008
			Young: 3D vs. 14D	<0.001
1B	*Ppargc1a* qPCR	2 way ANOVA with a Tukey correction for multiple comparisons	3D: Young vs. Aged	<0.001
			Young: TN vs. 3D	<0.001
			Young: TN vs. 14D	0.03
			Young: 3D vs. 14D	<0.001

2B	% tdTom%/Lin-;PDGFRa+	2 way ANOVA with an Uncorrected Fisher's LSD	Young: +/+ vs. CER/+	<0.001
			Aged: +/+ vs. CER/+	<0.001
2B	% PDGFRa+/Lin- cells	2 way ANOVA with an Uncorrected Fisher's LSD	Young: +/+ vs. CER/+	0.008
4B	*Adipoq* qPCR	2 way ANOVA with a Tukey correction for multiple comparisons	ICAM1: Young vs. Aged	<0.001
			Young: DPP4 vs. CD142	0.006
			Aged: DPP4 vs. ICAM1	<0.001
			Aged: DPP4+ vs. CD142	0.004
4B	*Fabp4* qPCR	2 way ANOVA with a Tukey correction for multiple comparisons	ICAM1: Young vs. Aged	<0.001
			Aged: DPP4 vs. ICAM1	<0.001
			Aged: ICAM1 vs. CD142	0.002
4D	*Adipoq* qPCR	2 way ANOVA with a Tukey correction for multiple comparisons	Young: DPP4 vs. CD142	0.03
			Young: ICAM1 vs. CD142	0.008
			Aged: DPP4 vs. ICAM1	0.04
			Aged: DPP4 vs. CD142	<0.001
			Aged: ICAM1 vs. CD142	0.006
4D	*Fabp4* qPCR	2 way ANOVA with a Tukey correction for multiple comparisons	ICAM1: Young vs. Aged	0.008
			Young: DPP4 vs. ICAM1	<0.001
			Young: DPP4 vs. CD142	<0.001
			Aged: DPP4 vs. ICAM1	<0.001
			Aged: DPP4+ vs. CD142	<0.001
			Aged: ICAM1 vs. CD142	0.03
4F	*Adipoq* qPCR	2 way ANOVA with an Uncorrected Fisher's LSD	Young: MIN vs. MAX	<0.001
			Aged: MIN vs. MAX	<0.001
4F	Fabp4 qPCR	2 way ANOVA with an Uncorrected Fisher's LSD	Young: MIN vs. MAX	<0.001
			Aged: MIN vs. MAX	<0.001
4G	*Ucp1* qPCR	2 way ANOVA with a Tukey correction for multiple comparisons	DPP4: Young vs. Young + Iso	<0.001
			DPP4: Aged vs. Aged + Iso	<0.001
			ICAM1: Young vs. Young + Iso	<0.001
			ICAM1: Aged vs. Aged + Iso	<0.001
			ICAM1: Young + Iso vs. Aged + Iso	0.02
			CD142: Young vs. Young + Iso	0.02
			CD142: Aged vs. Aged + Iso	<0.001
			Aged + Iso: Dpp4+ vs. Icam1+	0.002
			Aged + Iso: Icam1+ vs. Cd142+	0.03
4H	*Ucp1* qPCR	2 way ANOVA with a Tukey correction for multiple comparisons	MAX: Young vs. Young + Iso	<0.001
			MAX: Aged vs. Aged + Iso	<0.001
			Young + Iso: MIN vs. MAX	<0.001
			Aged + Iso: MIN vs. MAX	<0.001
6E	*Npr3* qPCR	2 way ANOVA with a Tukey correction for multiple comparisons	TN: Young vs. Aged	0.001
			14D: Young vs. Aged	0.01
			Young: TN vs. 14D	0.04
			Aged: TN vs. 3D	0.004

			Aged: TN vs. 14D	0.005
S1A	Body mass	2 way ANOVA with a Tukey correction for multiple comparisons	TN: Young vs. Aged	<0.001
			3D: Young vs. Aged	<0.001
			14D: Young vs. Aged	<0.001
S1B	iWAT mass	2 way ANOVA with a Tukey correction for multiple comparisons	TN: Young vs. Aged	0.005
			3D: Young vs. Aged	0.03
S1B	iWAT mass %	2 way ANOVA with a Tukey correction for multiple comparisons	No comparisons significant	N/A
S1E	*Ucp1* qPCR	2 way ANOVA with an Uncorrected Fisher's LSD	Young: TN vs. 14D	0.01
			Aged: TN vs. 14D	0.008
S1E	*Cidea* qPCR	2 way ANOVA with an Uncorrected Fisher's LSD	No comparisons significant	N/A
S4D	*Npr1* qPCR	2 way ANOVA with a Tukey correction for multiple comparisons	Young: TN vs. 3D	0.03
S4D	*Npr2* qPCR	2 way ANOVA with a Tukey correction for multiple comparisons	No comparisons significant	N/A
S4H	*Acly* qPCR	2 way ANOVA with a Tukey correction for multiple comparisons	3D: Young vs. Aged	<0.001
			14D: Young vs. Aged	<0.001
			Young: TN vs. 3D	<0.001
			Young: TN vs. 14D	<0.001
			Young: 3D vs. 14D	<0.001

722

723

References

Amiya Kumar Ghosh, M.O.B., Theresa Mau, Nathan Qi, and Raymond Yung (2019). Adipose Tissue Senescence and Inflammation in Aging is Reversed by the Young Milieu. J Gerontol A Biol Sci Med Sci *74*, 1709-1715.

Barreau, C., Labit, E., Guissard, C., Rouquette, J., Boizeau, M.L., Gani Koumassi, S., Carriere, A., Jeanson, Y., Berger-Muller, S., Dromard, C.*, et al.* (2016). Regionalization of browning revealed by whole subcutaneous adipose tissue imaging. Obesity (Silver Spring) *24*, 1081-1089.

Becher, T., Palanisamy, S., Kramer, D.J., Eljalby, M., Marx, S.J., Wibmer, A.G., Butler, S.D., Jiang, C.S., Vaughan, R., Schoder, H.*, et al.* (2021). Brown adipose tissue is associated with cardiometabolic health. Nat Med *27*, 58-65.

Benvie, A.M., Lee, D., Steiner, B.M., Xue, S., Jiang, Y., and Berry, D.C. (2023). Age-dependent Pdgfrbeta signaling drives adipocyte progenitor dysfunction to alter the beige adipogenic niche in male mice. Nat Commun *14*, 1806.

Berry, D.C., Jiang, Y., Arpke, R.W., Close, E.L., Uchida, A., Reading, D., Berglund, E.D., Kyba, M., and Graff, J.M. (2017). Cellular Aging Contributes to Failure of Cold-Induced Beige Adipocyte Formation in Old Mice and Humans. Cell Metab *25*, 166-181.

Berry, D.C., Jiang, Y., and Graff, J.M. (2016). Mouse strains to study cold-inducible beige progenitors and beige adipocyte formation and function. Nat Commun *7*, 10184.

Bordicchia, M., Liu, D., Amri, E.Z., Ailhaud, G., Dessi-Fulgheri, P., Zhang, C., Takahashi, N., Sarzani, R., and Collins, S. (2012). Cardiac natriuretic peptides act via p38 MAPK to induce the brown fat thermogenic program in mouse and human adipocytes. J Clin Invest *122*, 1022-1036.

Brosseau, C., Colas, L., Magnan, A., and Brouard, S. (2018). CD9 Tetraspanin: A New Pathway for the Regulation of Inflammation? Front Immunol *9*, 2316.

Burl, R.B., Ramseyer, V.D., Rondini, E.A., Pique-Regi, R., Lee, Y.H., and Granneman, J.G. (2018). Deconstructing Adipogenesis Induced by beta3-Adrenergic Receptor Activation with Single-Cell Expression Profiling. Cell Metab *28*, 300-309 e304.

Cannon, B., and Nedergaard, J. (2004). Brown Adipose Tissue: Function and Physiological Significance. Physiology Review *84*, 277–359.

Cederberg, A., Gronning, L.M., Ahren, B., Tasken, K., Carlsson, P., and Enerback, S. (2001). FOXC2 is a winged helix gene that counteracts obesity, hypertriglyceridemia, and diet-induced insulin resistance. Cell *106*, 563-573.

Chi, J., Wu, Z., Choi, C.H.J., Nguyen, L., Tegegne, S., Ackerman, S.E., Crane, A., Marchildon, F., Tessier-Lavigne, M., and Cohen, P. (2018). Three-Dimensional Adipose Tissue Imaging Reveals Regional Variation in Beige Fat Biogenesis and PRDM16-Dependent Sympathetic Neurite Density. Cell Metab *27*, 226-236 e223.

Chouchani, E.T., Kazak, L., and Spiegelman, B.M. (2019). New Advances in Adaptive Thermogenesis: UCP1 and Beyond. Cell Metab *29*, 27-37.

Chung, M.I., Bujnis, M., Barkauskas, C.E., Kobayashi, Y., and Hogan, B.L.M. (2018). Niche-mediated BMP/SMAD signaling regulates lung alveolar stem cell proliferation and differentiation. Development *145*.

764 Cohen, P., Levy, J.D., Zhang, Y., Frontini, A., Kolodin, D.P., Svensson, K.J., Lo, J.C., Zeng, X.,
765 Ye, L., Khandekar, M.J., *et al.* (2014). Ablation of PRDM16 and Beige Adipose Causes Metabolic
766 Dysfunction and a Subcutaneous to Visceral Fat Switch. Cell *156*, 304-316.

767 Coue, M., Barquissau, V., Morigny, P., Louche, K., Lefort, C., Mairal, A., Carpene, C., Viguerie,
768 N., Arner, P., Langin, D., *et al.* (2018). Natriuretic peptides promote glucose uptake in a cGMP-
769 dependent manner in human adipocytes. Sci Rep *8*, 1097.

770 Cypess, A.M., Chen, Y.C., Sze, C., Wang, K., English, J., Chan, O., Holman, A.R., Tal, I., Palmer,
771 M.R., Kolodny, G.M., *et al.* (2012). Cold but not sympathomimetics activates human brown
772 adipose tissue in vivo. Proc Natl Acad Sci U S A *109*, 10001-10005.

773 Cypess, A.M., Lehman, S., Williams, G., Tal, I., Rodman, D., Goldfine, A.B., Kuo, F.C., Palmer,
774 E.L., Tseng, Y.H., Doria, A., *et al.* (2009). Identification and importance of brown adipose tissue
775 in adult humans. N Engl J Med *360*, 1509-1517.

776 Dichamp, J., Barreau, C., Guissard, C., Carriere, A., Martinez, Y., Descombes, X., Penicaud, L.,
777 Rouquette, J., Casteilla, L., Plouraboue, F., *et al.* (2019). 3D analysis of the whole subcutaneous
778 adipose tissue reveals a complex spatial network of interconnected lobules with heterogeneous
779 browning ability. Sci Rep *9*, 6684.

780 Drokhlyansky, E., Smillie, C.S., Van Wittenberghe, N., Ericsson, M., Griffin, G.K., Eraslan, G.,
781 Dionne, D., Cuoco, M.S., Goder-Reiser, M.N., Sharova, T., *et al.* (2020). The Human and Mouse
782 Enteric Nervous System at Single-Cell Resolution. Cell *182*, 1606-1622 e1623.

783 Ferrero, R., Rainer, P., and Deplancke, B. (2020). Toward a Consensus View of Mammalian
784 Adipocyte Stem and Progenitor Cell Heterogeneity. Trends Cell Biol *30*, 937-950.

785 Fleming, S.J., Chaffin, M.D., Arduini, A., Akkad, A.-D., Banks, E., Marioni, J.C., Philippakis,
786 A.A., Ellinor, P.T., and Babadi, M. (2022). CellBender remove-background: a deep generative
787 model for unsupervised removal of background noise from scRNA-seq datasets. bioRxiv.

788 Gentili, A., Frangione, M.R., Albini, E., Vacca, C., Ricci, M.A., De Vuono, S., Boni, M., Rondelli,
789 F., Rotelli, L., Lupattelli, G., *et al.* (2017). Modulation of natriuretic peptide receptors in human
790 adipose tissue: molecular mechanisms behind the "natriuretic handicap" in morbidly obese
791 patients. Transl Res *186*, 52-61.

792 Gesta, S., Tseng, Y.H., and Kahn, C.R. (2007). Developmental origin of fat: tracking obesity to its
793 source. Cell *131*, 242-256.

794 Goldberg, E.L., Shchukina, I., Youm, Y.H., Ryu, S., Tsusaka, T., Young, K.C., Camell, C.D.,
795 Dlugos, T., Artyomov, M.N., and Dixit, V.D. (2021). IL-33 causes thermogenic failure in aging
796 by expanding dysfunctional adipose ILC2. Cell Metab *33*, 2277-2287 e2275.

797 Goncalves, L.F., Machado, T.Q., Castro-Pinheiro, C., de Souza, N.G., Oliveira, K.J., and
798 Fernandes-Santos, C. (2017). Ageing is associated with brown adipose tissue remodelling and loss
799 of white fat browning in female C57BL/6 mice. Int J Exp Pathol *98*, 100-108.

800 Graja, A., Garcia-Carrizo, F., Jank, A.M., Gohlke, S., Ambrosi, T.H., Jonas, W., Ussar, S., Kern,
801 M., Schurmann, A., Aleksandrova, K., *et al.* (2018). Loss of periostin occurs in aging adipose
802 tissue of mice and its genetic ablation impairs adipose tissue lipid metabolism. Aging Cell *17*,
803 e12810.

804 Jaitin, D.A., Adlung, L., Thaiss, C.A., Weiner, A., Li, B., Descamps, H., Lundgren, P., Bleriot, C.,
805 Liu, Z., Deczkowska, A., *et al.* (2019). Lipid-Associated Macrophages Control Metabolic
806 Homeostasis in a Trem2-Dependent Manner. Cell *178*, 686-698 e614.

807 Jespersen, N.Z., Larsen, T.J., Peijs, L., Daugaard, S., Homoe, P., Loft, A., de Jong, J., Mathur, N.,
808 Cannon, B., Nedergaard, J., *et al.* (2013). A classical brown adipose tissue mRNA signature partly
809 overlaps with brite in the supraclavicular region of adult humans. Cell Metab *17*, 798-805.

810 Kovacova, Z., Tharp, W.G., Liu, D., Wei, W., Xie, H., Collins, S., and Pratley, R.E. (2016).
811 Adipose tissue natriuretic peptide receptor expression is related to insulin sensitivity in obesity and
812 diabetes. Obesity (Silver Spring) *24*, 820-828.

813 Lee, Y.H., Kim, S.N., Kwon, H.J., and Granneman, J.G. (2017). Metabolic heterogeneity of
814 activated beige/brite adipocytes in inguinal adipose tissue. Sci Rep *7*, 39794.

815 Li, B., Gould, J., Yang, Y., Sarkizova, S., Tabaka, M., Ashenberg, O., Rosen, Y., Slyper, M.,
816 Kowalczyk, M.S., Villani, A.C., *et al.* (2020). Cumulus provides cloud-based data analysis for
817 large-scale single-cell and single-nucleus RNA-seq. Nat Methods *17*, 793-798.

818 Long, J.Z., Svensson, K.J., Tsai, L., Zeng, X., Roh, H.C., Kong, X., Rao, R.R., Lou, J., Lokurkar,
819 I., Baur, W., *et al.* (2014). A smooth muscle-like origin for beige adipocytes. Cell Metab *19*, 810-
820 820.

821 Marcelin, G., Ferreira, A., Liu, Y., Atlan, M., Aron-Wisnewsky, J., Pelloux, V., Botbol, Y.,
822 Ambrosini, M., Fradet, M., Rouault, C., *et al.* (2017). A PDGFRalpha-Mediated Switch toward
823 CD9(high) Adipocyte Progenitors Controls Obesity-Induced Adipose Tissue Fibrosis. Cell Metab
824 *25*, 673-685.

825 Martinez Calejman, C., Trefely, S., Entwisle, S.W., Luciano, A., Jung, S.M., Hsiao, W., Torres,
826 A., Hung, C.M., Li, H., Snyder, N.W., *et al.* (2020). mTORC2-AKT signaling to ATP-citrate lyase
827 drives brown adipogenesis and de novo lipogenesis. Nat Commun *11*, 575.

828 McDonald, M.E., Li, C., Bian, H., Smith, B.D., Layne, M.D., and Farmer, S.R. (2015). Myocardin-
829 related transcription factor a regulates conversion of progenitors to beige adipocytes. Cell *160*,
830 105-118.

831 Merrick, D., Sakers, A., Irgebay, Z., Okada, C., Calvert, C., Morley, M.P., Percec, I., and Seale,
832 P. (2019). Identification of a mesenchymal progenitor cell hierarchy in adipose tissue. Science
833 *364*.

834 Moro, C., Galitzky, J., Sengenes, C., Crampes, F., Lafontan, M., and Berlan, M. (2004). Functional
835 and pharmacological characterization of the natriuretic peptide-dependent lipolytic pathway in
836 human fat cells. J Pharmacol Exp Ther *308*, 984-992.

837 Mottillo, E.P., Balasubramanian, P., Lee, Y.H., Weng, C., Kershaw, E.E., and Granneman, J.G.
838 (2014). Coupling of lipolysis and de novo lipogenesis in brown, beige, and white adipose tissues
839 during chronic beta3-adrenergic receptor activation. J Lipid Res *55*, 2276-2286.

840 Nguyen, H.P., Lin, F., Yi, D., Xie, Y., Dinh, J., Xue, P., and Sul, H.S. (2021). Aging-dependent
841 regulatory cells emerge in subcutaneous fat to inhibit adipogenesis. Dev Cell *56*, 1437-1451 e1433.

842 Pfannenberg, C., Werner, M.K., Ripkens, S., Stef, I., Deckert, A., Schmadl, M., Reimold, M.,
843 Haring, H.U., Claussen, C.D., and Stefan, N. (2010). Impact of age on the relationships of brown
844 adipose tissue with sex and adiposity in humans. Diabetes *59*, 1789-1793.

Prabata, A., Ikeda, K., Rahardini, E.P., Hirata, K.I., and Emoto, N. (2021). GPNMB plays a protective role against obesity-related metabolic disorders by reducing macrophage inflammatory capacity. J Biol Chem *297*, 101232.

Rogers, N.H., Landa, A., Park, S., and Smith, R.G. (2012). Aging leads to a programmed loss of brown adipocytes in murine subcutaneous white adipose tissue. Aging cell *11*, 1074-1083.

Rosell, M., Kaforou, M., Frontini, A., Okolo, A., Chan, Y.W., Nikolopoulou, E., Millership, S., Fenech, M.E., MacIntyre, D., Turner, J.O*., et al.* (2014). Brown and white adipose tissues: intrinsic differences in gene expression and response to cold exposure in mice. American journal of physiology Endocrinology and metabolism *306*, E945-964.

Rosenwald, M., Perdikari, A., Rulicke, T., and Wolfrum, C. (2013). Bi-directional interconversion of brite and white adipocytes. Nat Cell Biol *15*, 659-667.

Saade, M., Araujo de Souza, G., Scavone, C., and Kinoshita, P.F. (2021). The Role of GPNMB in Inflammation. Front Immunol *12*, 674739.

Saito, M., Okamatsu-Ogura, Y., Matsushita, M., Watanabe, K., Yoneshiro, T., Nio-Kobayashi, J., Iwanaga, T., Miyagawa, M., Kameya, T., Nakada, K*., et al.* (2009). High incidence of metabolically active brown adipose tissue in healthy adult humans: effects of cold exposure and adiposity. Diabetes *58*, 1526-1531.

Sakers, A., De Siqueira, M.K., Seale, P., and Villanueva, C.J. (2022). Adipose-tissue plasticity in health and disease. Cell *185*, 419-446.

Sanchez-Gurmaches, J., Tang, Y., Jespersen, N.Z., Wallace, M., Martinez Calejman, C., Gujja, S., Li, H., Edwards, Y.J.K., Wolfrum, C., Metallo, C.M*., et al.* (2018). Brown Fat AKT2 Is a Cold-Induced Kinase that Stimulates ChREBP-Mediated De Novo Lipogenesis to Optimize Fuel Storage and Thermogenesis. Cell Metab *27*, 195-209 e196.

Seale, P., Conroe, H.M., Estall, J., Kajimura, S., Frontini, A., Ishibashi, J., Cohen, P., Cinti, S., and Spiegelman, B.M. (2011). Prdm16 determines the thermogenic program of subcutaneous white adipose tissue in mice. J Clin Invest *121*, 96-105.

Sengenès, C., Berlan, M., Glisezinski, I., Lafontan, M., and Galitzky, J. (2000). Natriuretic peptides: a new lipolytic pathway in human adipocytes. The FASEB Journal *14*, 1345-1351.

Sengenes, C., Bouloumie, A., Hauner, H., Berlan, M., Busse, R., Lafontan, M., and Galitzky, J. (2003). Involvement of a cGMP-dependent pathway in the natriuretic peptide-mediated hormone-sensitive lipase phosphorylation in human adipocytes. J Biol Chem *278*, 48617-48626.

Shamsi, F., Piper, M., Ho, L.L., Huang, T.L., Gupta, A., Streets, A., Lynes, M.D., and Tseng, Y.H. (2021). Vascular smooth muscle-derived Trpv1(+) progenitors are a source of cold-induced thermogenic adipocytes. Nat Metab *3*, 485-495.

Shao, M., Ishibashi, J., Kusminski, C.M., Wang, Q.A., Hepler, C., Vishvanath, L., MacPherson, K.A., Spurgin, S.B., Sun, K., Holland, W.L*., et al.* (2016). Zfp423 Maintains White Adipocyte Identity through Suppression of the Beige Cell Thermogenic Gene Program. Cell Metab *23*, 1167-1184.

Shao, M., Wang, Q.A., Song, A., Vishvanath, L., Busbuso, N.C., Scherer, P.E., and Gupta, R.K. (2019). Cellular Origins of Beige Fat Cells Revisited. Diabetes *68*, 1874-1885.

885 Slyper, M., Porter, C.B.M., Ashenberg, O., Waldman, J., Drokhlyansky, E., Wakiro, I., Smillie,
886 C., Smith-Rosario, G., Wu, J., Dionne, D., *et al.* (2020). A single-cell and single-nucleus RNA-
887 Seq toolbox for fresh and frozen human tumors. Nat Med *26*, 792-802.

888 St-Onge, M.-P. (2005). Relationship between body composition changes and changes in physical
889 function and metabolic risk factors in aging. Current Opinion in Clinical Nutrition and Metabolic
890 Care *8*, 523–528.

891 Stine, R.R., Shapira, S.N., Lim, H.W., Ishibashi, J., Harms, M., Won, K.J., and Seale, P. (2016).
892 EBF2 promotes the recruitment of beige adipocytes in white adipose tissue. Mol Metab *5*, 57-65.

893 Ussar, S., Lee, K.Y., Dankel, S.N., Boucher, J., Haering, M.F., Kleinridders, A., Thomou, T., Xue,
894 R., Macotela, Y., Cypess, A.M., *et al.* (2014). ASC-1, PAT2, and P2RX5 are cell surface markers
895 for white, beige, and brown adipocytes. Sci Transl Med *6*, 247ra103.

896 Wang, Q.A., Tao, C., Gupta, R.K., and Scherer, P.E. (2013). Tracking adipogenesis during white
897 adipose tissue development, expansion and regeneration. Nat Med *19*, 1338-1344.

898 Wang, W., Ishibashi, J., Trefely, S., Shao, M., Cowan, A.J., Sakers, A., Lim, H.W., O'Connor, S.,
899 Doan, M.T., Cohen, P., *et al.* (2019). A PRDM16-Driven Metabolic Signal from Adipocytes
900 Regulates Precursor Cell Fate. Cell Metab *30*, 174-189 e175.

901 Wang, W., and Seale, P. (2016). Control of brown and beige fat development. Nat Rev Mol Cell
902 Biol *17*, 691-702.

903 Wu, J., Bostrom, P., Sparks, L.M., Ye, L., Choi, J.H., Giang, A.H., Khandekar, M., Virtanen, K.A.,
904 Nuutila, P., Schaart, G., *et al.* (2012). Beige adipocytes are a distinct type of thermogenic fat cell
905 in mouse and human. Cell *150*, 366-376.

906 Yoneshiro, T., Aita, S., Matsushita, M., Okamatsu-Ogura, Y., Kameya, T., Kawai, Y., Miyagawa,
907 M., Tsujisaki, M., and Saito, M. (2011). Age-related decrease in cold-activated brown adipose
908 tissue and accumulation of body fat in healthy humans. Obesity (Silver Spring) *19*, 1755-1760.

909 Yu, X.X., Lewin, D.A., Forrest, W., and Adams, S.H. (2002). Cold elicits the simultaneous
910 induction of fatty acid synthesis and beta-oxidation in murine brown adipose tissue: prediction
911 from differential gene expression and confirmation in vivo. FASEB journal : official publication
912 of the Federation of American Societies for Experimental Biology *16*, 155-168.

913 Zheng, G.X., Terry, J.M., Belgrader, P., Ryvkin, P., Bent, Z.W., Wilson, R., Ziraldo, S.B.,
914 Wheeler, T.D., McDermott, G.P., Zhu, J., *et al.* (2017). Massively parallel digital transcriptional
915 profiling of single cells. Nat Commun *8*, 14049.

916